Supplementary Information

Iron clusters and single atom sites cooperatively promote bifunctional oxygen reaction activity in ultra-stable flexible zinc-air battery

Qi Liu,‡[a] Panzhe Qiao,‡[cde] Di Shen,[b] Ying Xie,[b] Baoluo Wang,[b] Tianyu Han,[b] Hongtu Shi,[b] Lei Wang,*[b] and Honggang Fu*[ab]

[a] Key Laboratory of Superlight Materials and Surface Technology of the Ministry of Education of the People's Republic of China, Harbin Engineering University, Harbin, 150001, China. E-mail: fuhg@vip.sina.com, fuhg@hlju.edu.cn.

[b] Key Laboratory of Functional Inorganic Material Chemistry, Ministry of Education of the People's Republic of China, Heilongjiang University, Harbin, 150080, China. E-mail: wanglei0525@hlju.edu.cn.

[c] Shanghai Synchrotron Radiation Facility, Shanghai Advanced Research Institute, Chinese Academy of Sciences, Shanghai, 201210, China.

[d] Shanghai Institute of Applied Physics, Chinese Academy of Science, Shanghai, 201210, China

[e] University of Chinese Academy of Sciences, Beijing, 100049, China.

‡ The authors contribute the work equally.

1. Experimental Section

1.1 Chemicals

$FeCl_3$ (AR), $LiClO_4$ (99.99 %), Na_2CO_3 (AR), Pyrrole (99 %), KOH (95 %), $Zn(OAC)_2$ (99 %) polyvinyl alcohol (99 %), Acrylamide (99 %), N,N′-methylenebisacrylamide (99 %), Potassium persulfate (99.99 %), Ethylene glycol (AR), RuO_2 (99.9 %) were purchased from Aladdin. Commercial Pt/C (20 wt%) and carbon cloth were purchased from Shanghai Hesen Electric Co., Ltd. All the chemicals are in analytic grade and used without further purification.

1.2 Synthesis

1.2.1 Pretreatment of CC

The pre-treatment of carbon cloth (CC) involves two processes. Firstly, the CC is cut into 2 × 2 cm sizes. Then, it is respectively sonicated in acetone and distilled water for 0.5 h. Finally, the CC is immersed in a 0.1 M HCl solution (pH = 1.05) for 0.5 h, resulting in the treated CC.

1.2.2 Synthesis of PPy/CC

The process of synthesizing polypyrrole on a CC substrate (PPy/CC) via an electrodeposition strategy using the electrolyte composed of 1.05 g $LiClO_4$, 2.10 g Na_2CO_3, 1.0 mL pyrrole and 90 mL deionized water (pH = 11.38). A three-electrode system was used, with CC as the working electrode, Ag/AgCl electrode as the reference electrode, and Pt electrode as the counter electrode. Electrodeposition was conducted at a constant potential of 0.9 V for 10 min, the PPy/CC was prepared. For comparison, the electrodeposition voltage was changed to 0.8 and 1.0 V, and the corresponding samples were designed as PPy/CC-0.8 and PPy/CC-1.0, respectively.

1.2.3 Synthesis of Fe_{SA}/Fe_{AC}@PPy/CC

The synthesis of Fe_{SA}/Fe_{AC}@PPy/CC was achieved through a one-step cyclic voltammetry electrodeposition method. A solution containing 200 μM $FeCl_3$ dissolved in deionized water served as the electrolyte (pH = 3.33). The process utilized a three-electrode system, with the PPy/CC as the working electrode, an Ag/AgCl electrode as the reference electrode and a graphite rod electrode as the counter electrode. The voltage ranging from −0.6 to 0.2 V was cycled for 20 cycles to obtain the sample named Fe_{SA}/Fe_{AC}@PPy/CC. For comparison, the CV was varied to 10 and 30 cycles to prepare Fe@PPy/CC-10 and Fe@PPy/CC-30, respectively. We also utilized PPy/CC-0.8 and PPy/CC-1.0 as substrates for iron species electrodeposition, designated as Fe_{SA}/Fe_{AC}@PPy/CC-0.8 and Fe_{SA}/Fe_{AC}@PPy/CC-1.0, respectively.

1.3 Synthesis of gel-polymer electrolytes (GPEs)

1.3.1 Synthesis of PVA GPE

First, 1.0 g polyvinyl alcohol (PVA) powder was dissolved in 10 mL deionized water (pH = 6.11) and then heated up to 90 °C. After the solution was completely transferred to transparent gel, 3 mL mixture solution of 6 M KOH contained 0.2 M $Zn(OAC)_2$ (pH = 14.95) solution was added. After stirring for another 20 min, the mixture was poured onto a 3 cm × 3 cm plastic box and then froze in a freezer at −20 ℃ for a night. The PVA GPE could be successfully obtained after melting at room temperature.

1.3.2 Synthesis of PAM GPE

We synthesized polyacrylamide (PAM) GPE using a thermal polymerization method. The PAM GPE were prepared as follows: 4.5 g of acrylamide (AM), 4.5 mg of N,N′-methylenebisacrylamide (MBAA, crosslinking agent), and 10 mg of potassium persulfate ($K_2S_2O_8$, initiator) were dissolved in 10 mL of deionized water (pH = 6.94) and continuously stirred until the solid dissolved. The resulting solution was poured into a 3 cm × 3 cm plastic box, which was then placed in an oven at 60 °C for 2 h. Subsequently, the as-prepared PAM GPE were immersed in the electrolyte of a 6 M KOH solution with 0.2 M $Zn(OAC)_2$ (pH = 14.95) for 72 h before use.

1.3.3 Synthesis of PAM/EG GPE

The synthesis of polyacrylamide/ethylene glycol (PAM/EG) GPE is similar to that of PAM GPE, using the same free radical polymerization method. The polymerization process is as follows: 4.5 g of AM, 4.5 mg of MBAA and 10 mg of $K_2S_2O_8$ were dissolved in 4.5 mL of deionized water and 5.5 mL of EG (pH = 6.81) and continuously stirred until the solid dissolved. The resulting solution was poured into a 3 cm × 3 cm plastic box, which was then placed in an oven at 60 °C for 2 h. Subsequently, the as-prepared PAM/EG GPE were immersed in a 6 M KOH solution with 0.2 M $Zn(OAC)_2$ (pH = 14.95) for 72 h before use.

1.4 Characterizations

Scanning electron microscopy (SEM) images were obtained by a Hitachi S-4800 instrument operating at 5 kV. Transmission electron microscopy (TEM) imaging was performed on a JEM-2100 electron microscope with an acceleration voltage of 200 kV. The atom-resolved HAADF-STEM were recorded on a JEOL ARM200F microscope (cold-field emission) operated at 200 kV. X-ray diffraction (XRD) patterns were collected on a Bruker D8 Advance diffractometer equipped with Cu Kα (λ = 1.5406 Å) radiation and a LynxEye Detector. X-ray photoelectron spectroscopy (XPS) was conducted with a Mg Kα achromatic X-ray source. Using inductively coupled plasma optical emission spectrometry (Agilent 725 ICP-OES) to determine the contents of Fe. The XAFS was performed on BL14W1 of the Shanghai Synchrotron Radiation Facility (SSRF) of China with a Si (111) double-crystal monochromator. The self-supporting materials require distinct treatments for various characterizations. It can be directly utilized for XRD, SEM and XAFS characterizations. For TEM analyses, the self-supporting electrode is immersed in ethanol and subjected to ultrasonic treatment, after which the solution is dropped onto the surface of microgrid. For XPS testing, the catalyst must be scraped from the CC support. In ICP-OES, the scraped catalyst is first dissolved in aqua regia and then diluted before further detection. The tension and pressure data of gel electrolyte were collected by an tensile testing machine (Beijing JiTai Tech Detection Device Co.,Ltd, JITAI-W100N). The differential scanning calorimetry (DSC) was performed at a differential scanning calorimeter (Netzsch DSC 214 polyma) between –100 and 20 °C with a cooling/heating rate of 5 °C min^{-1}.

1.5 Electrochemical measurement

1.5.1 Electrochemical measurements of OER and ORR

All the electrochemical measurements were estimated by a standard three electrode system at 25 ℃. The oxygen evolution reaction (OER) performances were tested on a CHI660E electrochemical workstation in 1.0 M KOH (pH = 14.07) electrolyte. The as-prepared 1 cm × 1 cm self-supported electrode, carbon rod electrode and saturated calomel electrode (SCE) were used as the working electrode, counter electrode and reference electrode, respectively. For the preparation of the RuO_2/CC electrode, 2 mg of RuO_2 powder was dispersed in a mixed solution comprising 1.5 mL of ethanol and 0.5 mL of 0.5% Nafion, followed by ultrasonic dispersion. Subsequently, 100 μL of the catalyst slurry was drop-coated onto a 1 cm × 1 cm CC substrate to construct the RuO_2/CC electrode.

The potential was calibrated to reversible hydrogen electrode (RHE) based on the Nernst equation, and the current density was normalized to the effective geometrical surface area (1.0 cm^2):

$$E\ (\text{V vs. RHE}) = E\ (\text{V vs. SCE}) + 0.097 + 0.0592 \times \text{pH}$$

Cyclic voltammetry (CV) curves were recorded by different scan rates from 10 to 50 mV s^{-1} to determine the double layer capacitance (C_{dl}). The electrochemical active surface area (ECSA) was determined based on C_{dl} using the following formula:

$$ECSA = \frac{C_{dl}}{C_s}$$

in which an ideal planar electrode has a C_{dl} of 40 μF cm^{-2} defined as C_{s} = 40 μF cm^{-2}.

A Pine instrument (US) was used to ORR measurements in O_2-saturated 0.1 M KOH (pH = 12.87) electrolyte. Platinum foil (1.0 cm^2) and reversible hydrogen electrode (RHE) were employed as counter electrode and reference electrode. For preparation of working electrode: We scrape the catalyst off the CC, and then 5 mg of the powder was uniformly dispersed into 1.5 mL ethanol and 0.5 mL of 0.5 % Nafion solution. 100 μL of the ink was dropped onto the glassy carbon disk of the RDE. Additionally, the LSV of the catalyst was measured by rotating ring–disk electrode (RRDE) with sweep rate of 5 mV

s^{-1} at different rotating speeds (400–2500 rpm min^{-1}). The current densities were calculated according to the CC area and the glassy carbon disk area, respectively.

1.5.2 Assembly and test of rechargeable Zn−air battery (ZAB)

The rechargeable aqueous ZAB was assembled using a self-supporting electrode as the air-cathode and a zinc plate measuring 2.5 cm × 4 cm with a thickness of 0.5 mm as the anode. Prior to assembly, the zinc plate must be polished to eliminate any surface oxide layer. Nickel foam was utilized as the current collector for the ZAB. The separator employed was a Celgard 3501 monolayer membrane featuring a microporous structure of 25 μm, which offers excellent resistance to alkaline solutions, high chemical and thermal stability, and robust antioxidant properties. The test device consisted of a homemade battery mold with a window area of 0.78 cm^2, using an electrolyte composed of a 6.0 M KOH and 0.2 M $Zn(OAC)_2$ solution (pH = 14.95). Cycling experiments were conducted in an environmental chamber at 25 °C and 101325 Pa. The ZAB cyclic performance was evaluated through repeated galvanostatic pulses, with each cycle comprising 30 min of discharging followed by 30 min of charging. The specific capacity and energy density were calculated according to the equation below.

$$\text{Specific capacity} = \frac{\text{current} \times \text{service hour}}{\text{weight of consumed Zn}}$$

$$\text{Energy density} = \frac{\text{current} \times \text{service hour} \times \text{average discharge voltage}}{\text{weight of consumed Zn}}$$

The FZAB was constructed by a typical sandwich-type structure. For the rechargeable FZAB, a 2 cm × 2 cm self-supporting electrode was used as an air-cathode, a 2.5 cm × 3 cm zinc plate was used as the anode. Prior to assembly, the zinc plate must be polished to eliminate any surface oxide layer. The prepared GPE serves as the electrolyte. The battery experiments are carried out in an environmental chamber at 40 ℃, 25 ℃, 0 ℃, −20 °C and −40 °C. The extreme low temperature FZABs measurements were conducted in the low-temperature test chamber (Zhejiang JIESHENG LOW-TEMP Equipment Co.,Ltd, DW-86W50). The charge-discharge cycle is comprised of 30 min discharging followed by a 30 min charging. All the batteries performances were evaluated in the atmospheric environment by using LAND CT2001A multichannel battery test system.

The ionic conductivity of the GPE was tested using a CHI660E electrochemical workstation. A GPE with an area of 1 × 1 cm was sandwiched between two nickel foams and fixed in place. A test program was set at (0.1–100 kHz with an amplitude of 5 mV) to measure the ohmic resistance. The equation for calculating the ionic conductivity (δ) is as follows:

$$\delta = \frac{L}{A \times R_b}$$

where L represents the GPEs thickness, A represents the GPEs area between the two nickel foams, R_b represents the bulk resistance of the GPEs. The R_b value is related to the intersection point of the real axis in AC impedance spectrum.

The electrolyte absorption and retention capacities of the synthesized GPEs were evaluated by monitoring the weight change over time. Specifically, the electrolyte retention ability was assessed under air exposure to expedite the testing process

The GPEs water absorption rate (W_t) was calculated according to the equationas follows:

$$W_t = \frac{W_1 - W_0}{W_0}$$

where W_0 corresponds to the weight of the GPEs, W_1 corresponds to the weight of wet GPEs after immersing in the liquid electrolyte for 72 h.

The GPEs water retention rate (W_t') was calculated according to the equation as follows:

$$W_t' = \frac{W_3}{W_2} \times 100\%$$

where W_2 represents the weight of the resulting GPEs and W_3 represents the weight of GPEs after being exposed to the testing environment for varying periods of time.

1.6 Computational methods

The density function theory (DFT) simulations are performed using CASTEP code. We adopt the plane wave basis with a cutoff energy of 340.0 eV, the self-consistent field (SCF) tolerance of 1×10^{-6} eV. All structures are fully optimized until the force on each ion is less than 0.03 eV/Å. The overpotentials (η) at various sites were calculated by the standard hydrogen electrode method developed by Nørskov et al.[1] The adsorption energies of O_2 on the surfaces of catalysts are defined as:

$$\Delta E^*_{O_2} = E_{O_2/\mathrm{surface}} - E_{O_2} - E_{\mathrm{surface}}$$

where $E_{O2/\mathrm{surface}}$, E_{O2}, and E_{surface} are the total energies of O_2 adsorbed surfaces, O_2 in the gas phase, and clean surfaces, respectively.

The free energies of H_2 and H_2O are calculated by placing them in a 10×10×10 cubic lattice, respectively. The following mechanisms for ORR were considered in our calculations:

$$* + O_2 + 2e^- + H_2O(l) + e^- \rightarrow *OOH + OH^- \qquad \triangle G_1$$

$$*OOH + e^- \rightarrow *O + OH^- \qquad \triangle G_2$$

$$*O + 2H^+ + 2e^- + H_2O \rightarrow *OH + OH^- \qquad \triangle G_3$$

$$*OH + e^- \rightarrow * + OH^- \qquad \triangle G_4$$

Overall reaction:

$$O_2(g)+2H_2O(l)+4e^- \rightarrow +4OH^-$$

The accurate free energy of *OOH, *O, *OH radicals in the electrolyte is difficult to obtain. By using the appropriate amount of $H_2O(g)$ and $H_2(g)$ relative to the stoichiometric amount, the free energy of adsorption $\Delta G*_{OOH}$, $\Delta G*_{O}$ and $\Delta G*_{OH}$ can be obtained.

$$\Delta G_{*OOH} = \Delta G(2H_2O(g)+* \rightarrow *OOH+\frac{3}{2}H_2(g))$$

$$= (E_{*OOH} + 1.5\times E_{H_2} - 2\times E_{H_2O} - E^{*}) + (E_{ZPE}(*OOH) + 1.5\times E_{ZPE}(H_2) - 2\times E_{ZPE}(H_2O) - E_{ZPE}(*)) - T\times(S_{*OOH} + 1.5\times S_{H_2} - 2\times S_{H_2O} - S_*)$$

$$\Delta G_{*O} = \Delta G(H_2O(g)+* \rightarrow *O+H_2(g))$$

$$= (E_{*O} + E_{H_2} - E_{H_2O} - E^{*}) + (E_{ZPE}(*O) + E_{ZPE}(H_2) - E_{ZPE}(H_2O) - E_{ZPE}(*)) - T\times(S_{*OOH} + S_{H_2} - S_{H_2O} - S_*)$$

$$\Delta G_{*OH} = \Delta G(H_2O(g)+* \rightarrow *OH+\frac{1}{2}H_2(g))$$

$$= (E_{*OH} + 0.5\times E_{H_2} - E_{H_2O} - E^{*}) + (E_{ZPE}(*OOH) + 0.5\times E_{ZPE}(H_2) - E_{ZPE}(H_2O) - E_{ZPE}(*)) - T\times(S_{*OOH} + 0.5\times S_{H_2} - S_{H_2O} - S_*)$$

where ΔG is the difference between free energies of the initial and final states:

$$\Delta G = \Delta E + \Delta ZPE - T\Delta S + \Delta G_U + \Delta G_{pH}$$

where *E* is the total energy calculated from DFT, Δ*ZPE* and Δ*S* are the corrected zero point energy and entropy at 298 K, respectively. $\Delta G_U = -\eta eU$, *U* is the applied potential and e is the transferred electron number. The Δ*ZPE* data are listed in **Table S7**. Because it is too hard to describe the O_2 with high-spin ground state, the Gibbs free energy of the O_2 is calculated based on the following formula with the experimental reaction energy of 4×1.23 eV= 4.92 eV.[2]

$$O_2(g)+2H_2(g) \rightarrow 2H_2O$$

Thus

$$G_{O_2}(g) = 2G_{H_2O}(l) - 2G_{H_2} + 4\times 1.23(eV)$$

The reaction free energy for ORR can be calculated using the following equations:

$$\Delta G_1 = \Delta G_{*OOH} - 4.92$$

$$\Delta G_2 = \Delta G_{*O} - \Delta G_{*OOH}$$

$$\Delta G_3 = \Delta G_{*OH} - \Delta G_{*O}$$

$$\Delta G_4 = -\Delta G_{*OH}$$

ΔG_{pH} is the correction for the free energy of H^+, expressed as by following formula:

$$\Delta G_{pH} = -k_B T \ln[H^+] = pH \times k_B T \ln 10$$

where k_B represents the Boltzmann constant, and T is the temperature under room conditions, specifically 273.15 K, with the value of ln10 being approximately 2.3026.

The binding energies (E_b) between GPEs and H_2O molecules were computed using the following equation:

$$E_b = E_{GPEs-H_2O} - E_{GPEs} - E_{H_2O}$$

in which E_{GPEs-H_2O} refers to the energy of the whole system, E_{GPEs} refers to the energy of the GPEs surface, and E_{H_2O} refers to the energy of the H_2O molecules.

2. Supplemental Figures and Tables

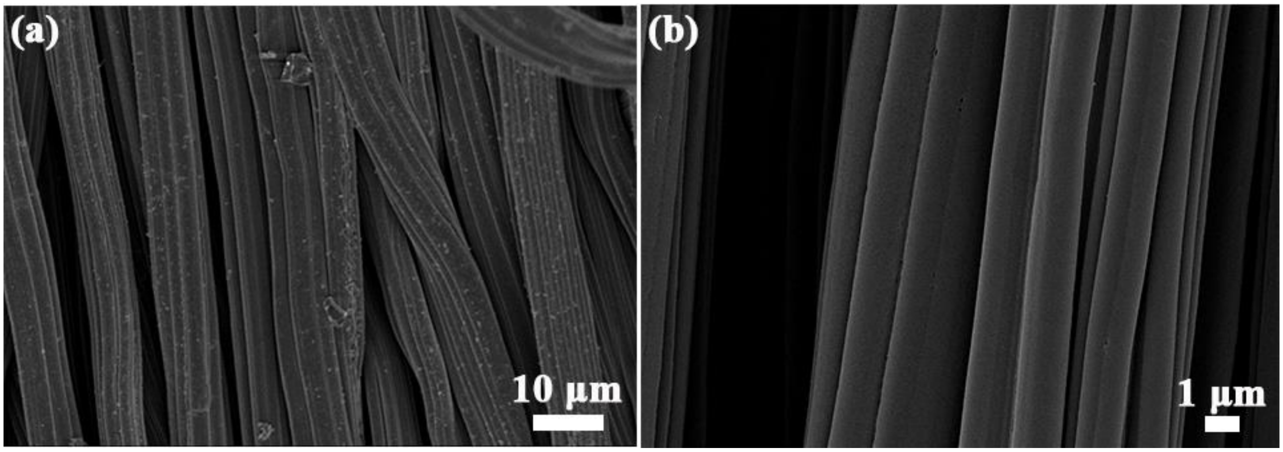

Fig. S1 SEM images of carbon cloth (CC) (a) before and (b) after pretreatment.

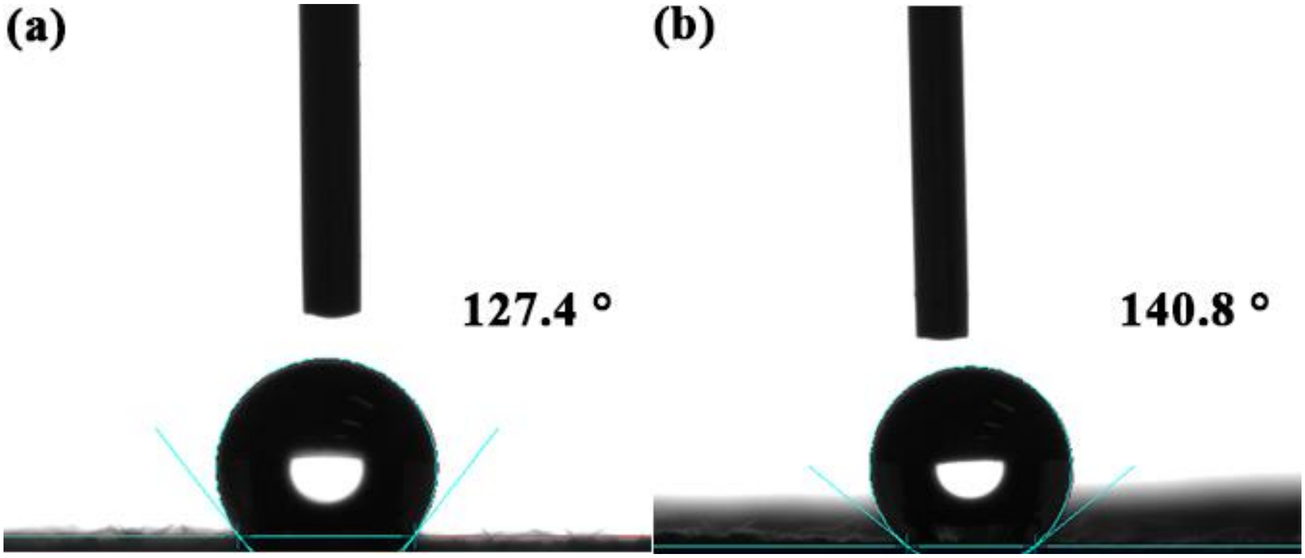

Fig. S2 Contact angle photos of CC (a) before and (b) after pretreatment.

In the synthesis process, the carbon cloth (CC) was pretreated with ethanol and hydrochloric acid to remove surface impurities. Due to hydrochloric acid is not a strong oxidant and does not improve the hydrophilicity, the treated CC could maintain its hydrophobicity after removal of impurity. This characterization is beneficial to the subsequent electrodeposition of polypyrrole (PPy).

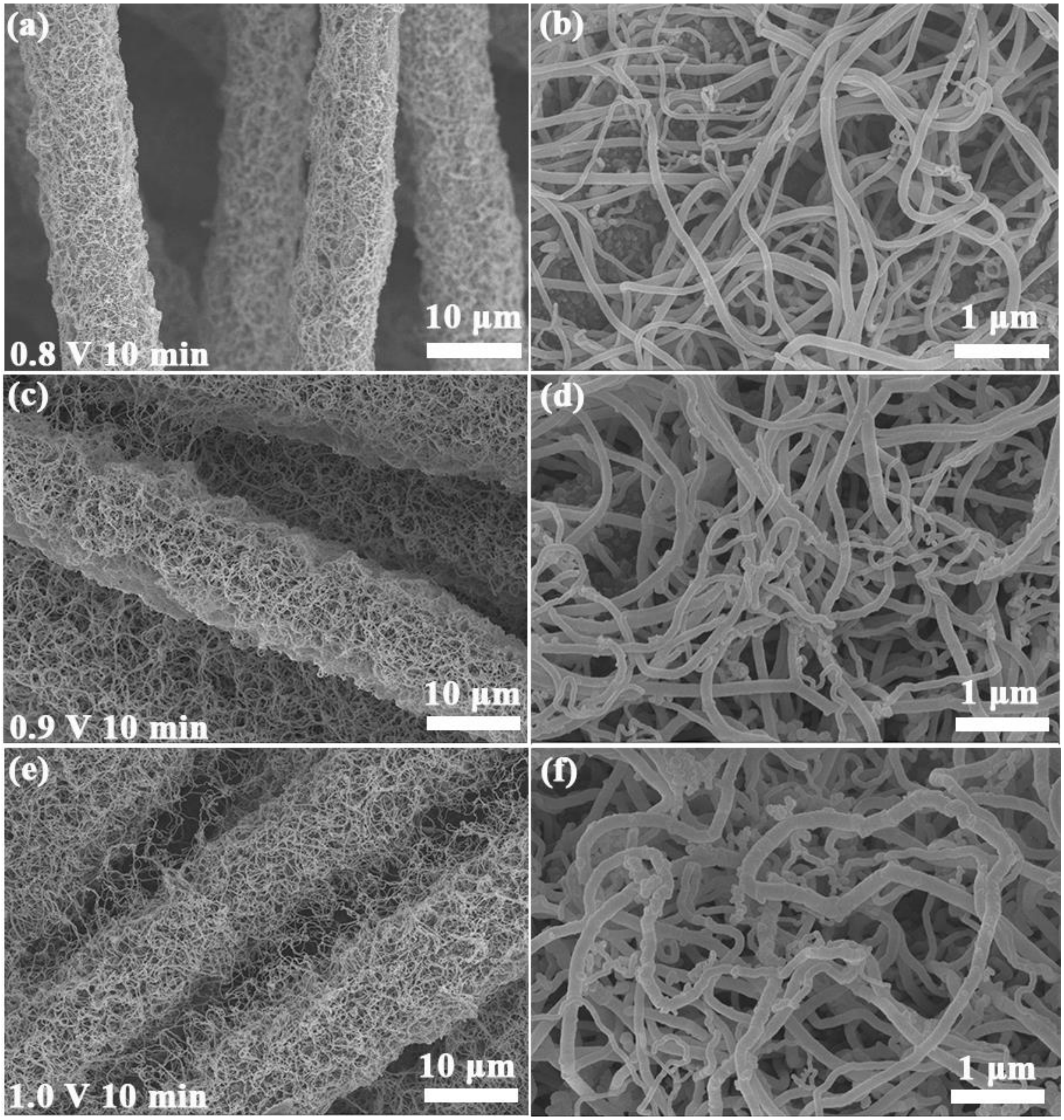

Fig. S3 SEM images of electrodeposition PPy on CC support at different applied potential: (a, b) PPy/CC-0.8 (at 0.8 V), (c, d) PPy/CC (at 0.9 V) and (e, f) PPy/CC-1.0 (at 1.0 V).

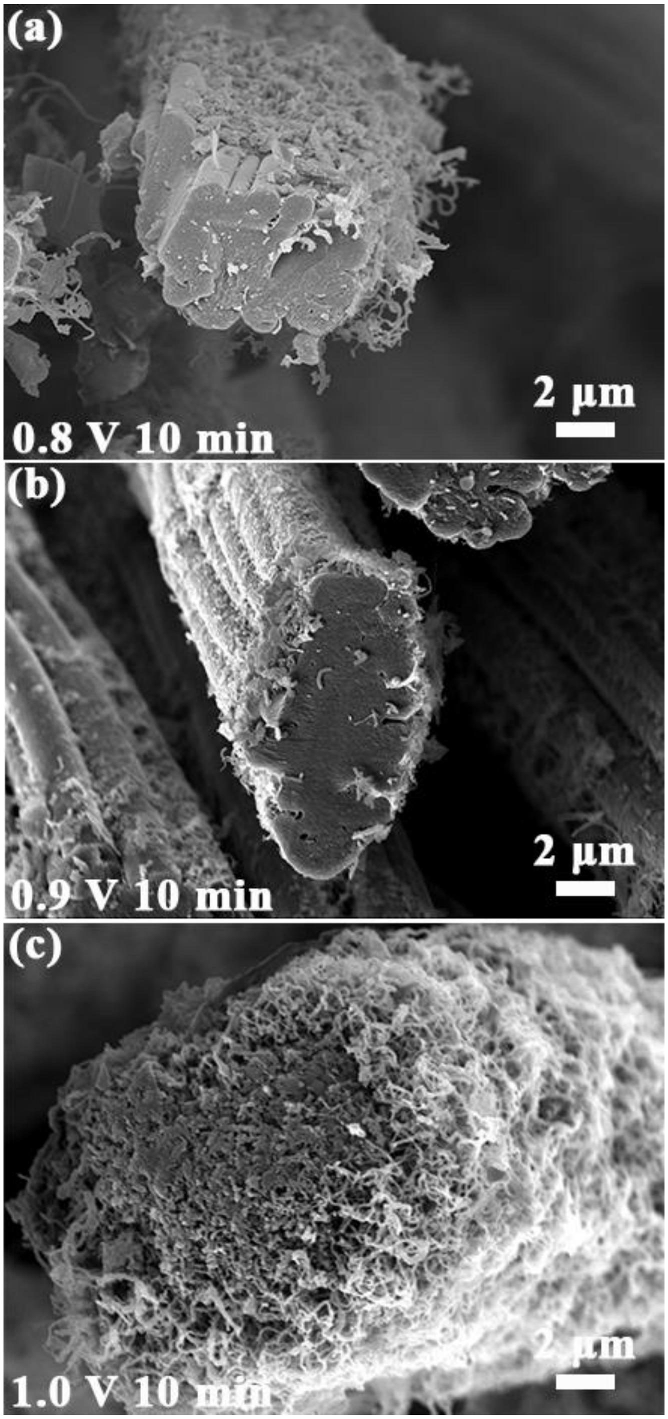

Fig. S4 SEM cross-sectional images of (a) PPy/CC-0.8, (b) PPy/CC and (c) PPy/CC-1.0.

The different applied potential for electrodeposition PPy on CC support was firstly investigate. As shown in **Fig. S3, S4**, the thickness the PPy is increased with the promote of electrodeposition voltage. Consequently, the PPy/CC with a moderate thickness of PPy synthesize at a deposition potential of 0.9 V was selected for further electrodeposition.

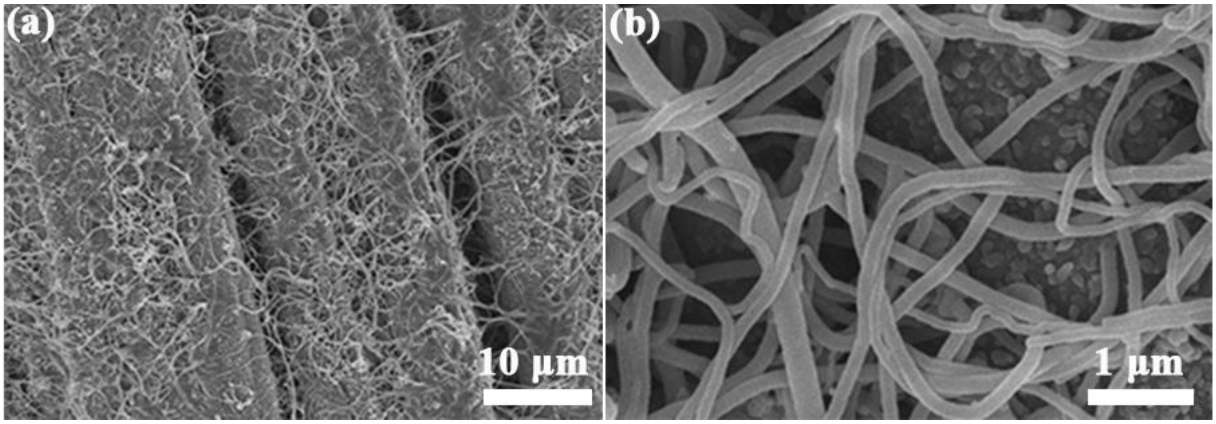

Fig. S5 SEM images of the sample prepared by untreated CC to electrodeposition PPy for 10 min at 0.9 V.

The untreated CC was under identical potential and time conditions. SEM images revealed extensive exposure of the CC surface, with markedly uneven growth of the tubular structures and the presence of particulate PPy (**Fig. S5**). Therefore, the untreated CC is not favorable for the electrodeposition of PPy.

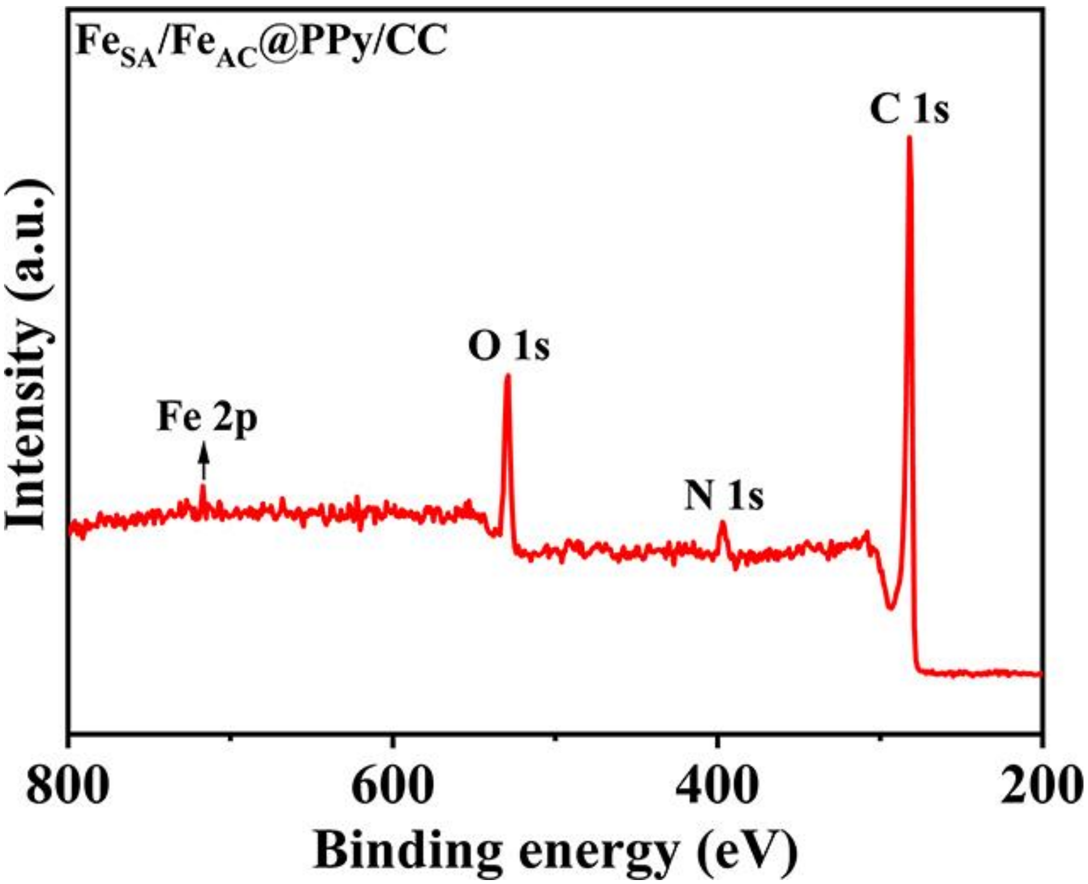

Fig. S6 Wide XPS spectrum of Fe$_{SA}$/Fe$_{AC}$@PPy/CC.

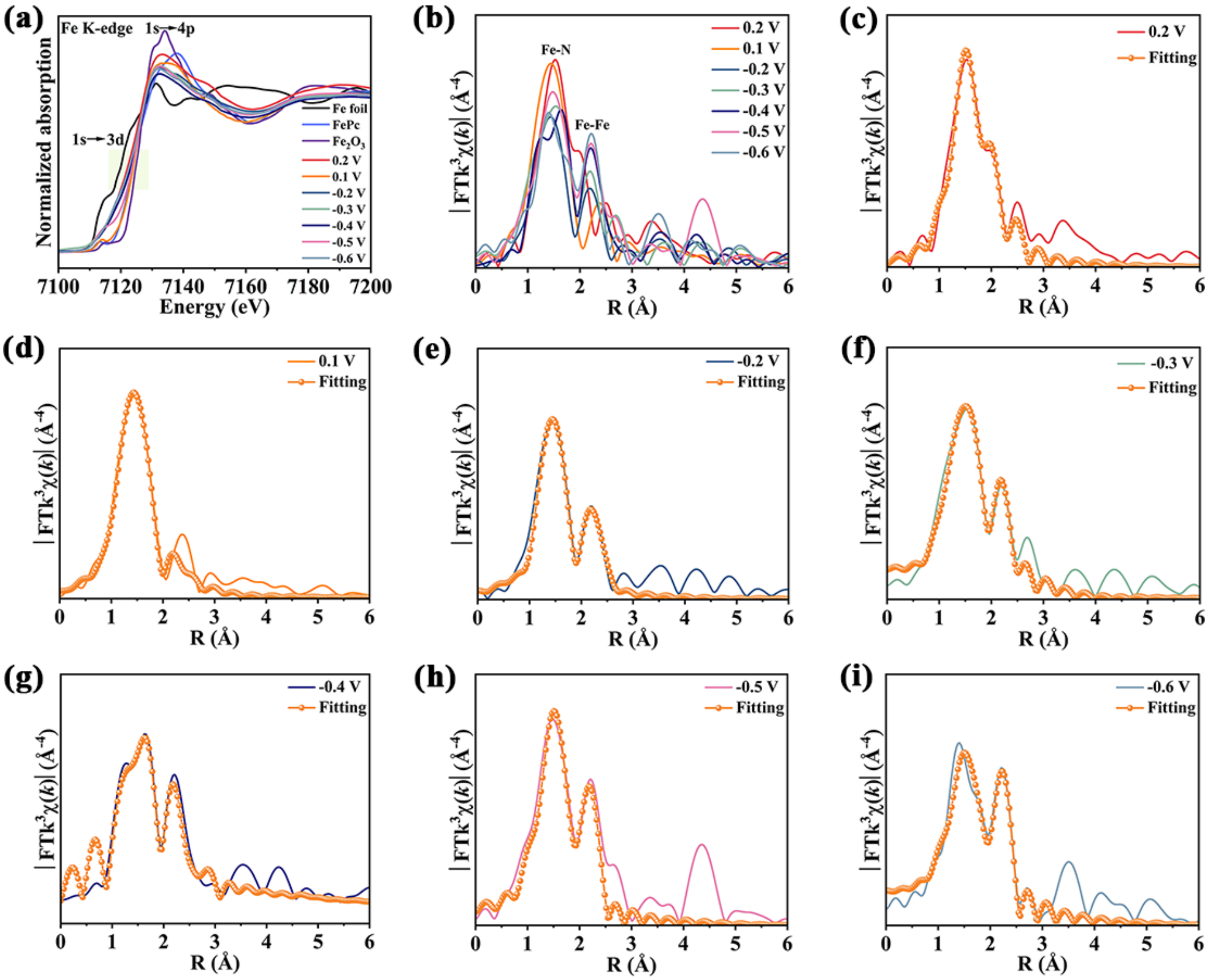

Fig. S7 XAFS spectra of the samples prepared through constant potential deposition of iron species on PPy/CC substrates at different potentials for 10 min. (a) The normalized Fe K-edge XANES and (b) FT-EXAFS spectra of the samples derived from different potentials. (c) FT-EXAFS fitting curves of Fe K-edge of the samples derived from (c) 0.2 V, (d) 0.1 V, (e) −0.2 V, (f) −0.3 V, (g) −0.4 V, (h) −0.5 V, and (i) −0.6 V.

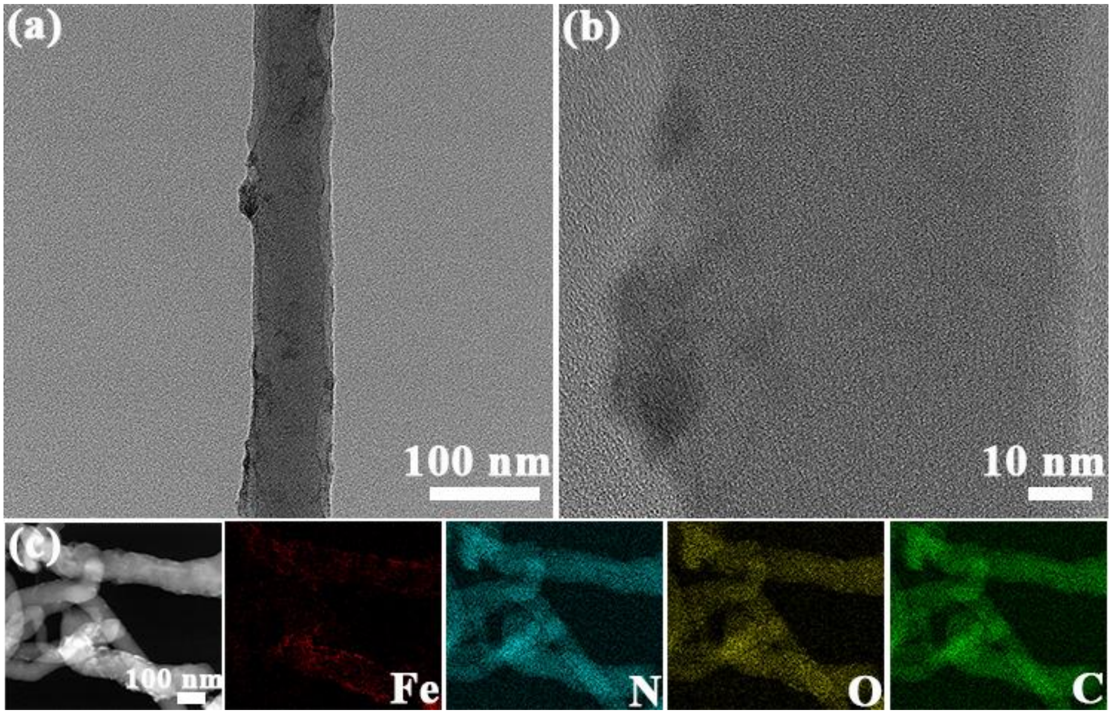

Fig. S8 (a) TEM, (b) HRTEM and (c) corresponding elemental mapping images of Fe@PPy/CC-10.

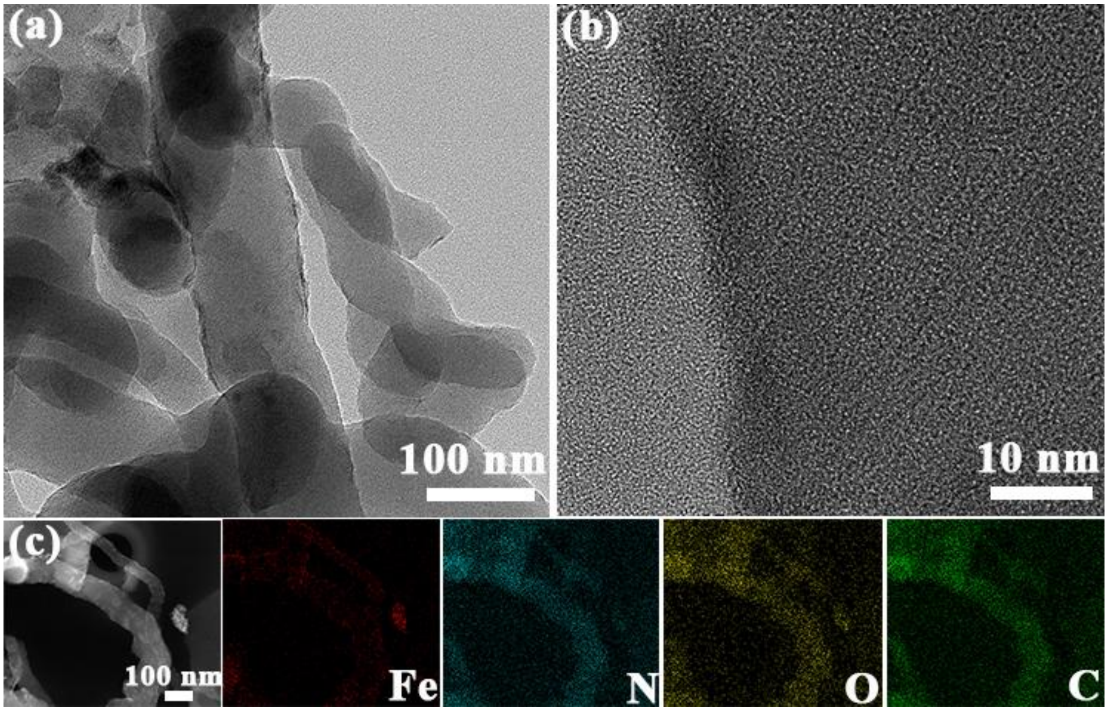

Fig. S9 (a) TEM, (b) HRTEM and (c) corresponding elemental mapping images of Fe@PPy/CC-30.

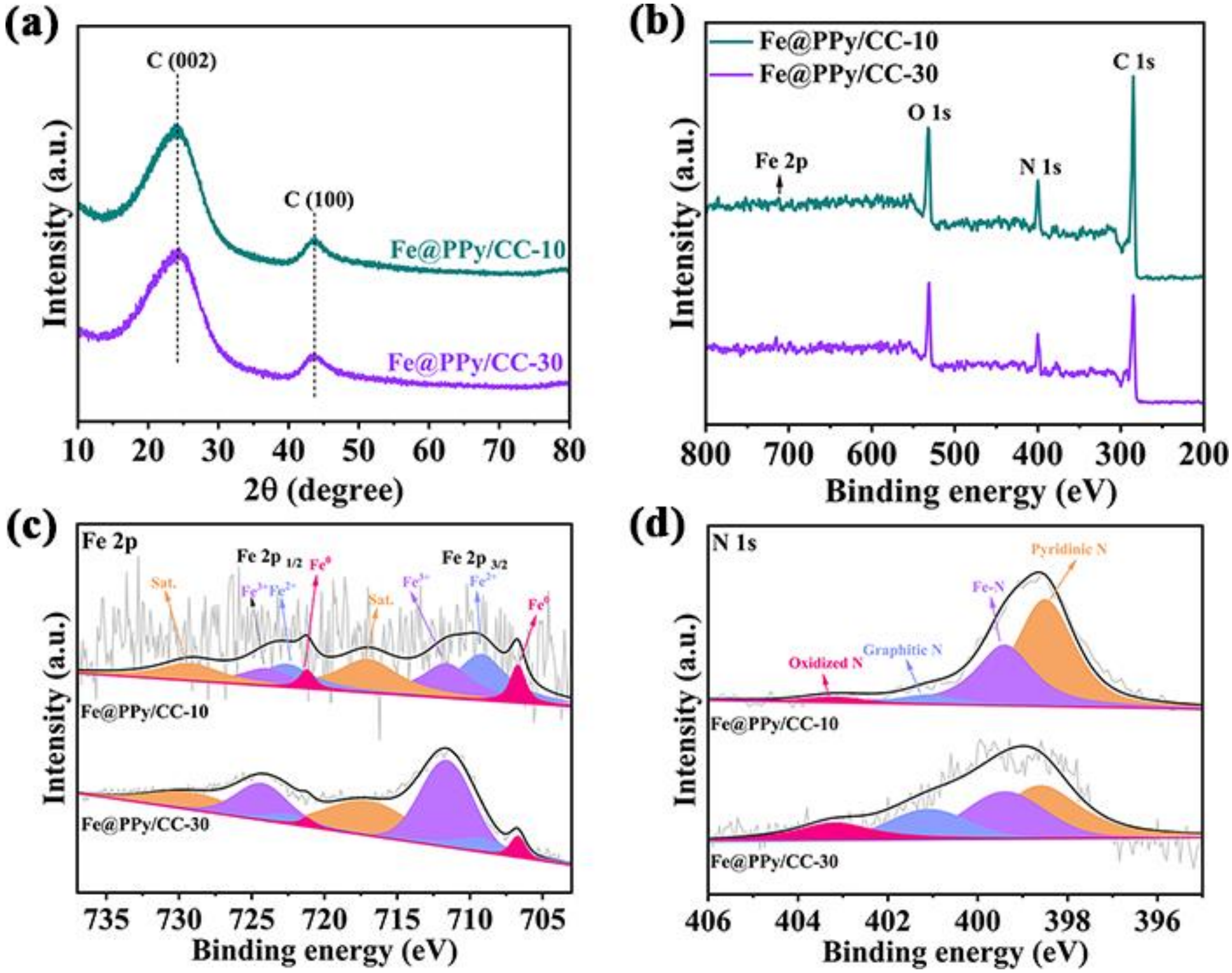

Fig. S10 (a) XRD. (b) Wide XPS spectra, (c) Fe 2p and (d) N 1s XPS spectra of Fe@PPy/CC-10 and Fe@PPy/CC-30.

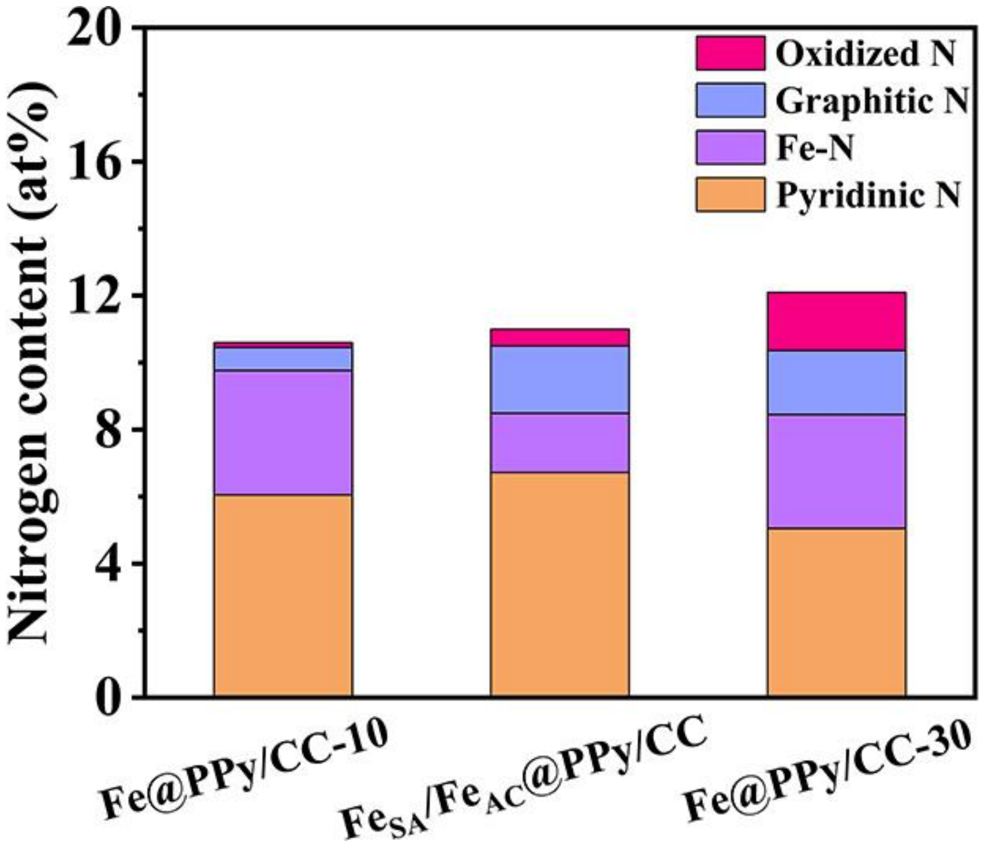

Fig. S11 Different N dopant contents diagrams of Fe@PPy/CC-10, Fe_{SA}/Fe_{AC}@PPy/CC and Fe@PPy/CC-30.

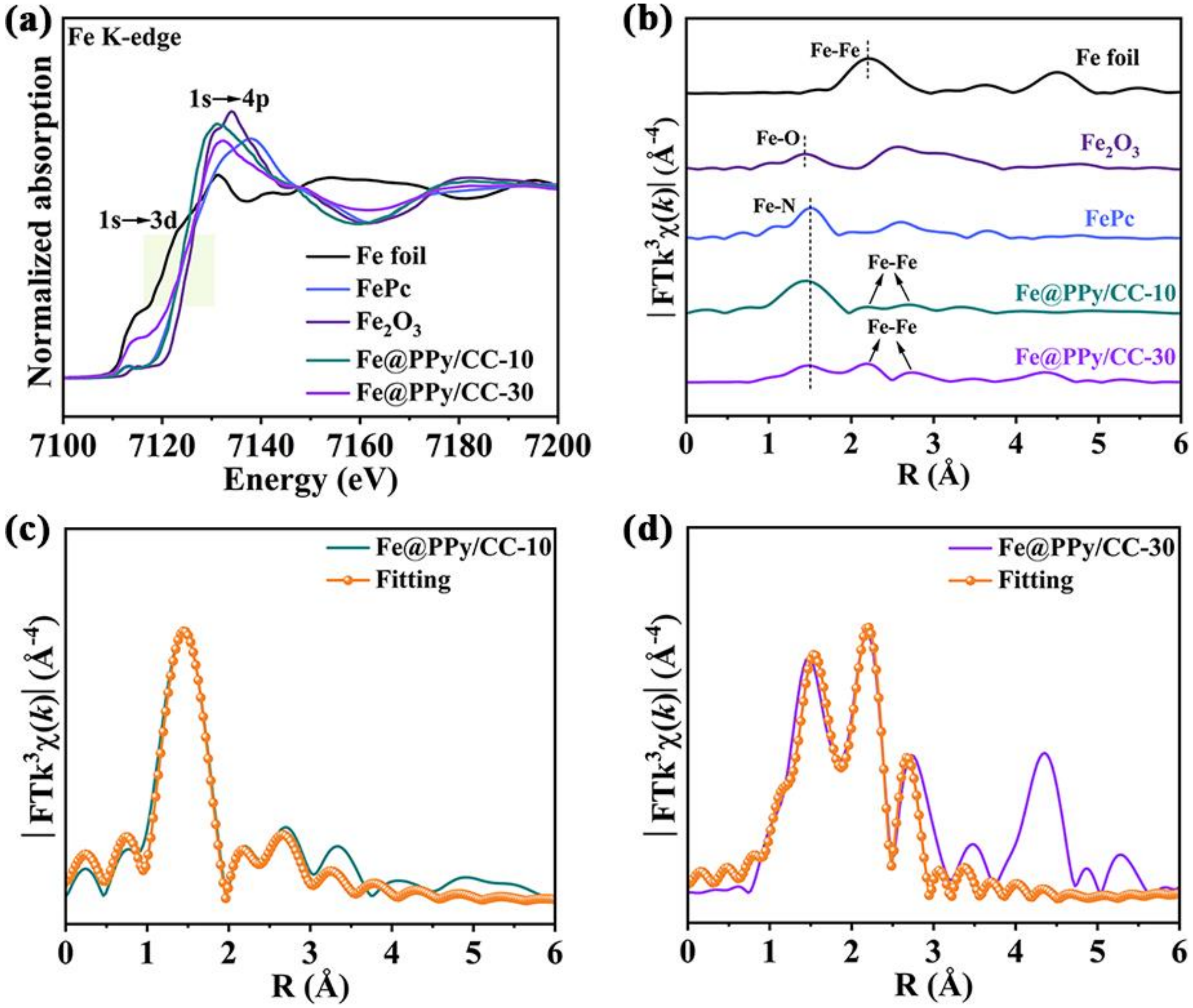

Fig. S12 (a) The normalized Fe K-edge XANES and (b) FT-EXAFS spectra of Fe foil, FePc, Fe_2O_3, Fe@PPy/CC-10 and Fe@PPy/CC-30. FT-EXAFS fitting curves of Fe K-edge for (c) Fe@PPy/CC-10 and (d) Fe@PPy/CC-30.

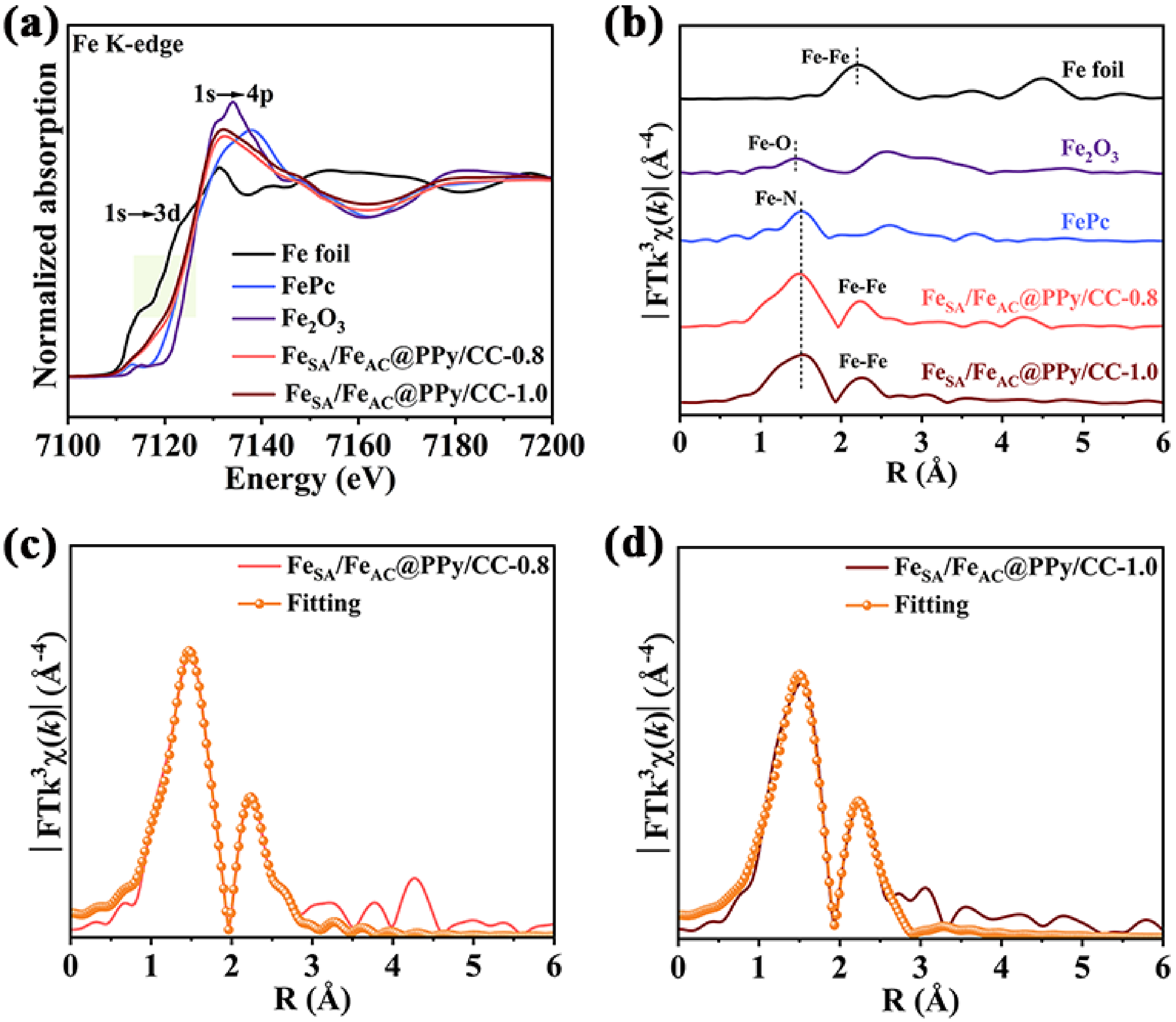

Fig. S13 (a) The normalized Fe K-edge XANES and (b) FT-EXAFS spectra of Fe foil, FePc, Fe_2O_3, Fe_{SA}/Fe_{AC}@PPy/CC-0.8 and Fe_{SA}/Fe_{AC}@PPy/CC-1.0. FT-EXAFS fitting curves of Fe K-edge for (c) Fe_{SA}/Fe_{AC}@PPy/CC-0.8 and (d) Fe_{SA}/Fe_{AC}@PPy/CC-1.0.

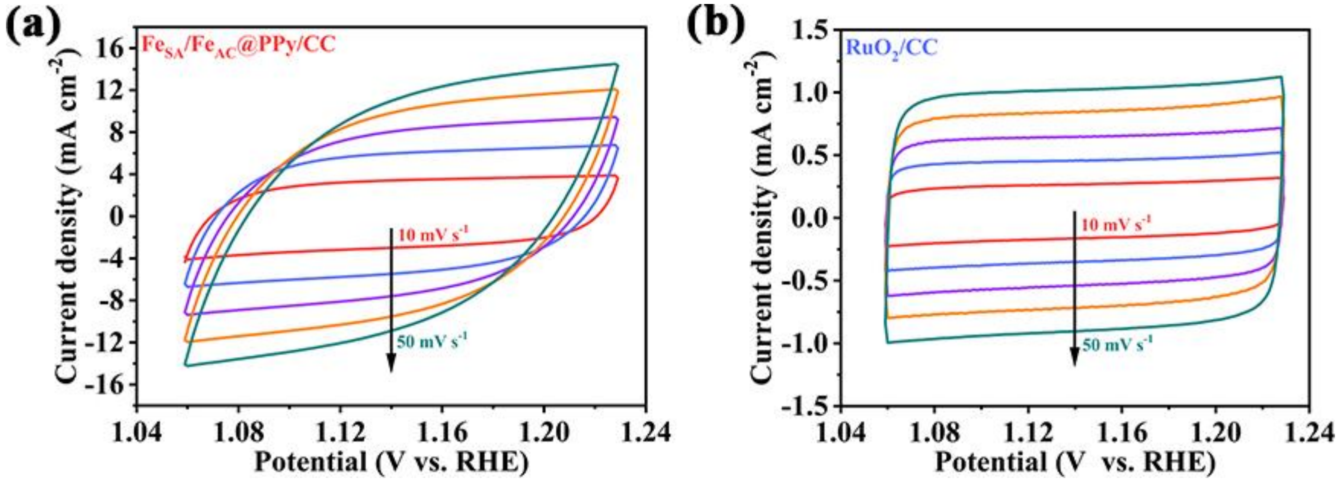

Fig. S14 CV curves of (a) Fe$_{SA}$/Fe$_{AC}$@PPy/CC and (b) RuO$_2$/CC at different scan rates of 10~50mV s^{-1}.

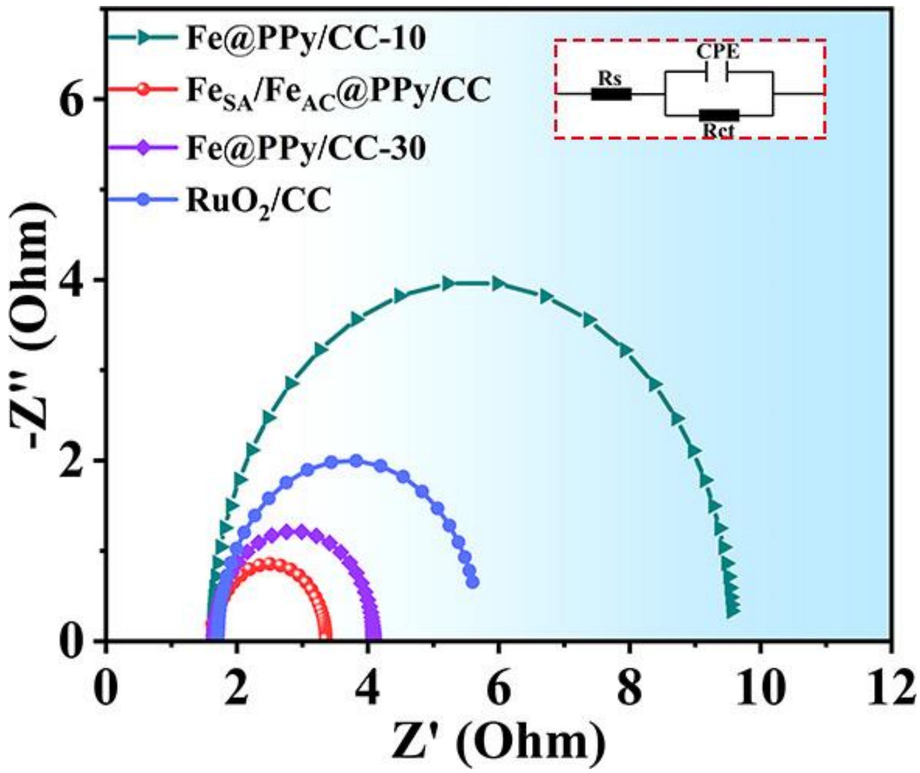

Fig. S15 EIS nyquist plots for all compared catalysts, while inset is the equivalent circuit.

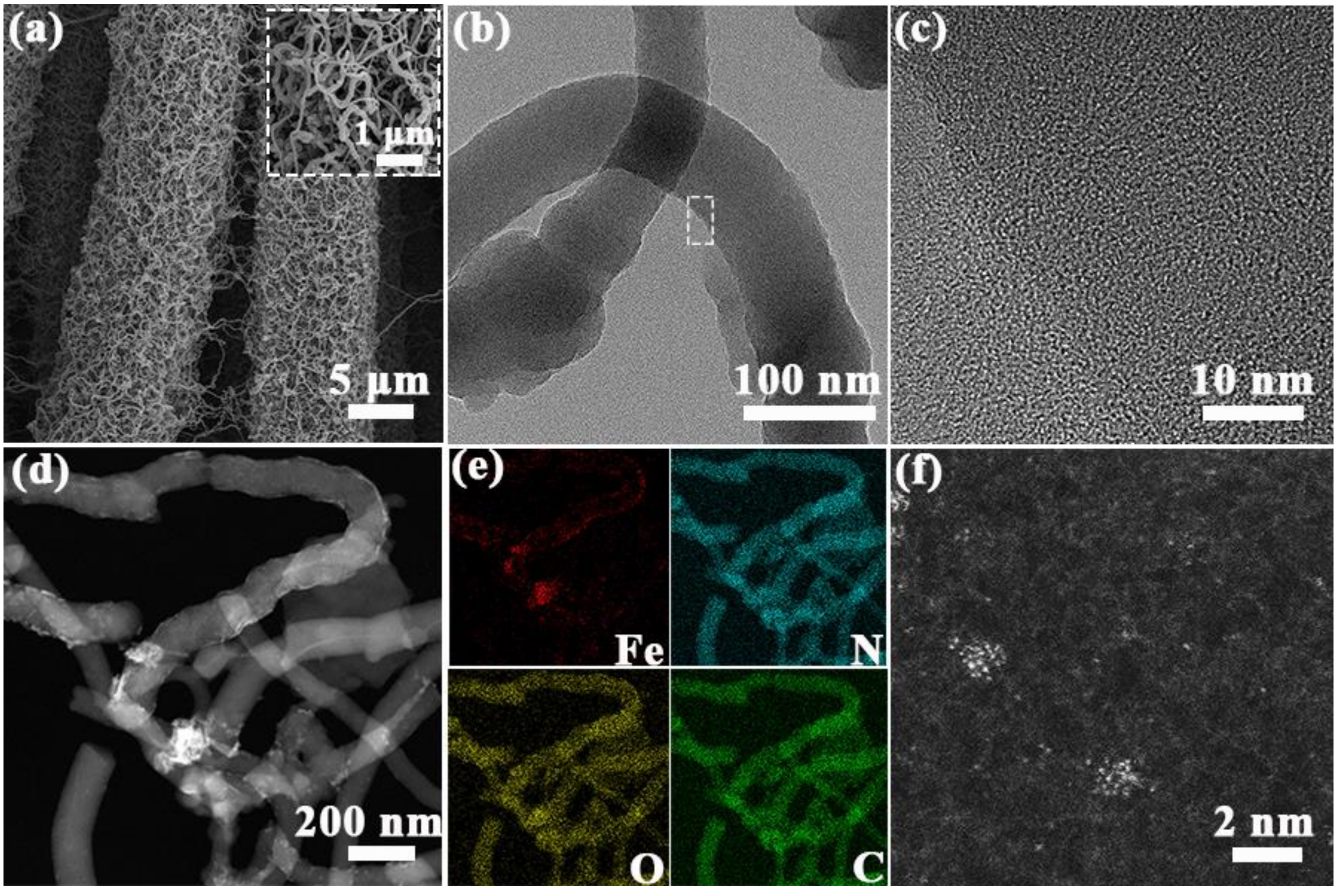

Fig. S16 (a) SEM, (b) TEM, (c) HRTEM, (d, e) elemental mapping and (f) HAADF-STEM images of Fe_{SA}/Fe_{AC}@PPy/CC after OER stability test.

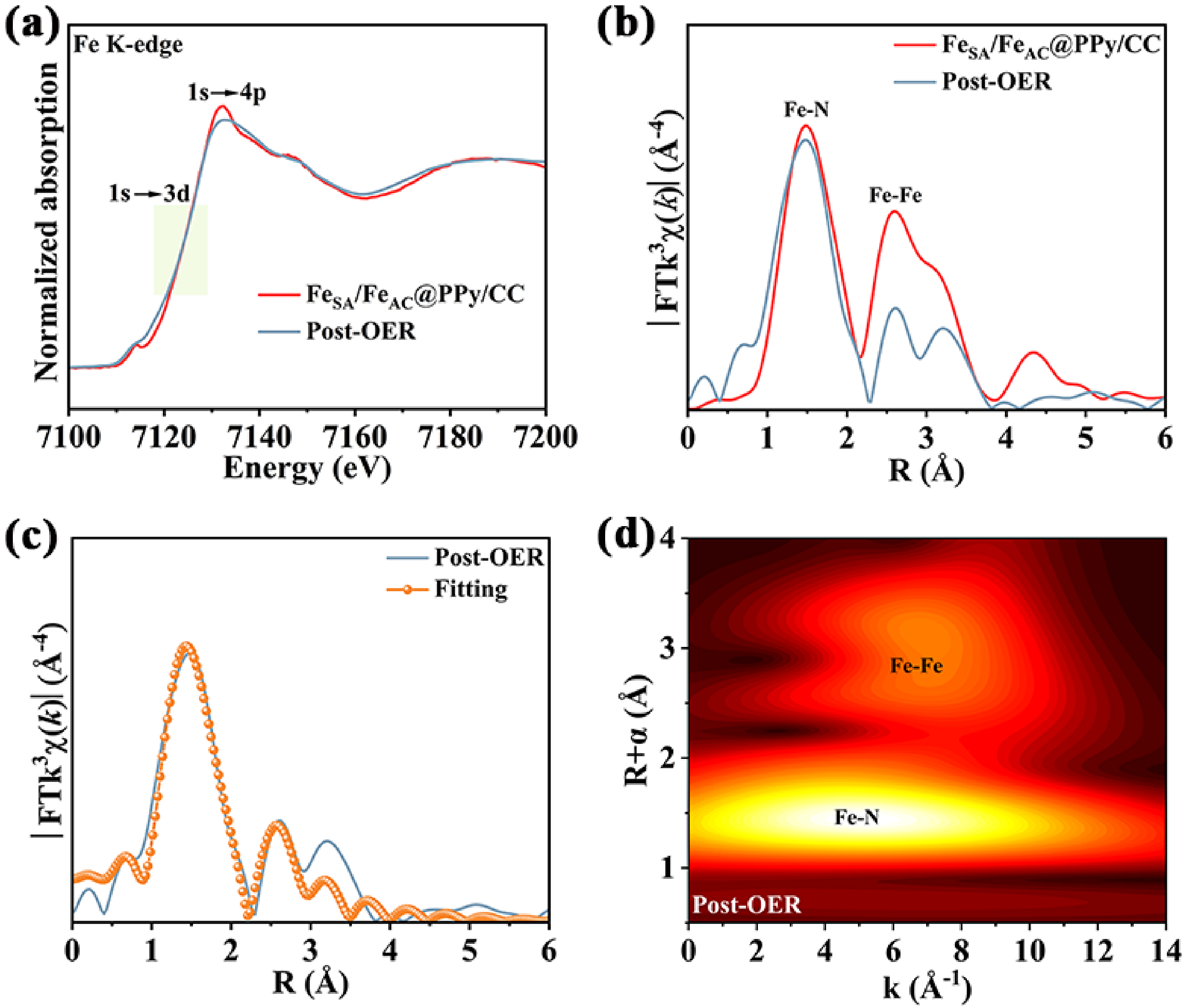

Fig. S17 (a) The normalized Fe K-edge XANES, (b) FT-EXAFS spectra and (c) corresponding fitting curves of Fe$_{SA}$/Fe$_{AC}$@PPy/CC before and after OER stability test. (d) WT count plots of Fe K-edge at K-space for Fe$_{SA}$/Fe$_{AC}$@PPy/CC after OER stability test.

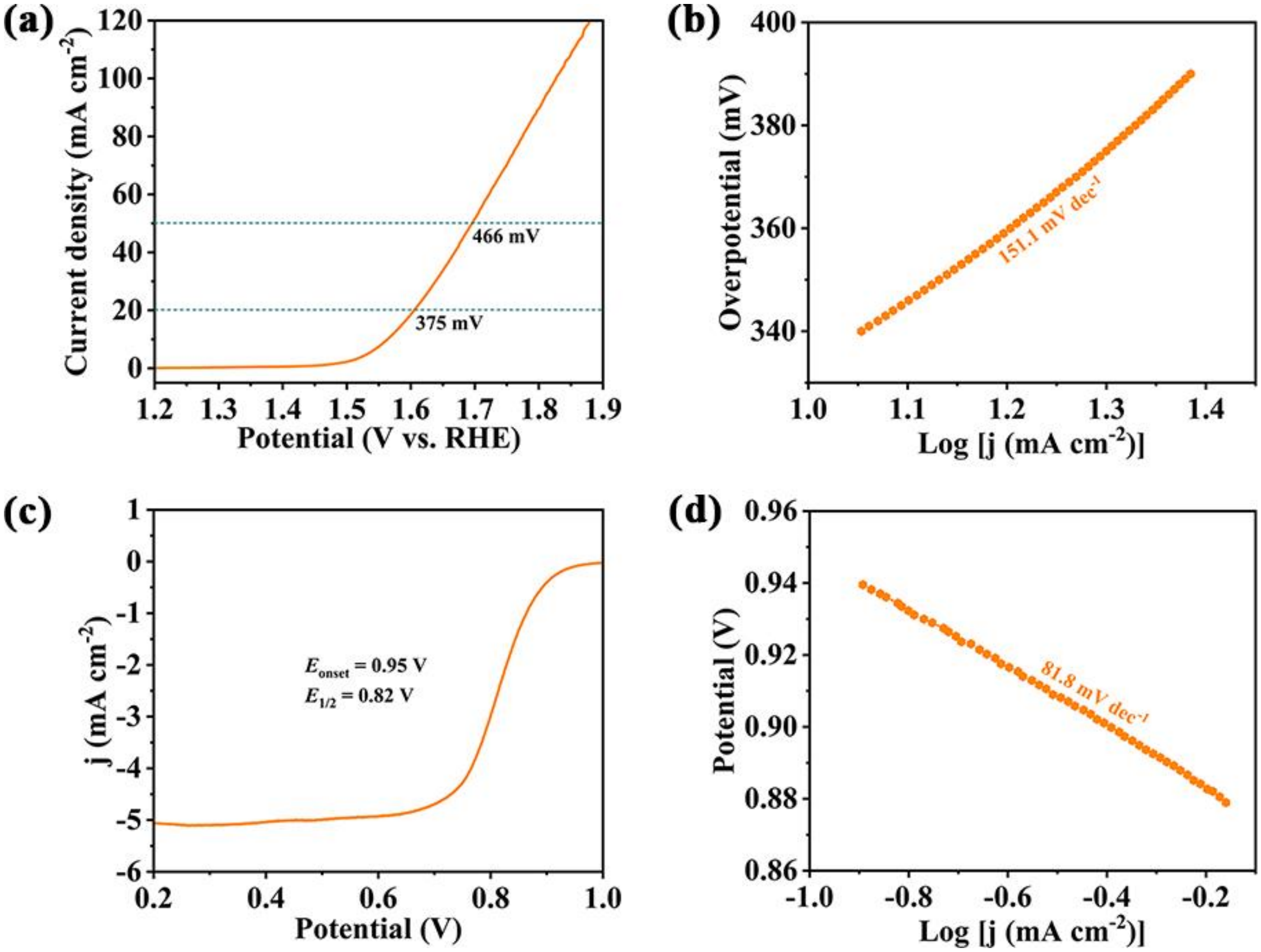

Fig. S18 Electrocatalytic performances of the sample prepared through constant potential deposition of iron species on PPy/CC substrates at 0.1 V for 10 min. (a) OER polarization curve and (b) corresponding Tafel plot. (c) ORR polarization curve and (d) corresponding Tafel plot.

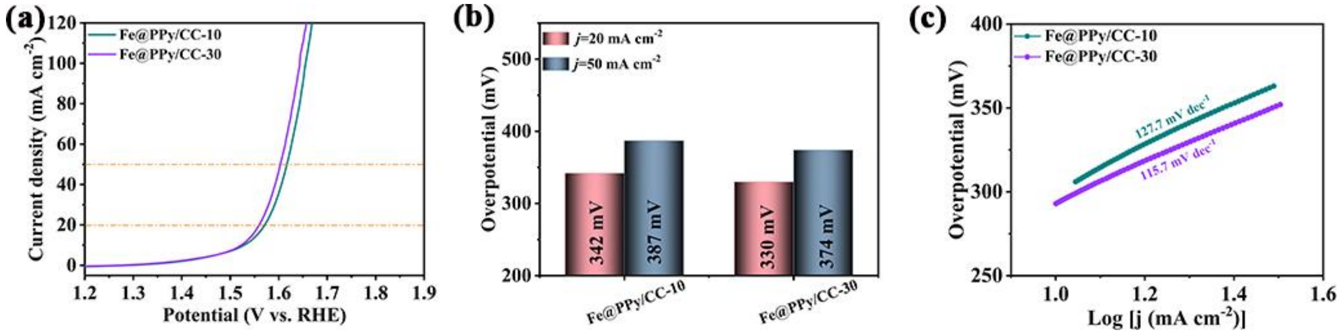

Fig. S19 (a) OER polarization curves, (b) the corresponding overpotentials at 20 and 50 mA cm^{-2}, and (c) Tafel plots of Fe@PPy/CC-10 and Fe@PPy/CC-30 tested in 1.0 M KOH electrolyte.

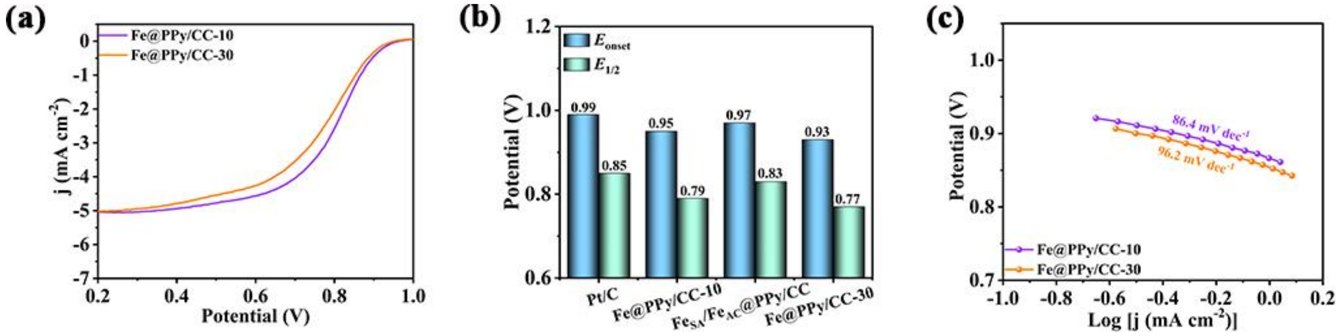

Fig. S20 (a) ORR polarization curves of Fe@PPy/CC-10 and Fe@PPy/CC-30 tested in 0.1 M KOH electrolyte. (b) E_{onset} and $E_{1/2}$ values of ORR for all compared catalysts. (c) Tafel plots of Fe@PPy/CC-10 and Fe@PPy/CC-30.

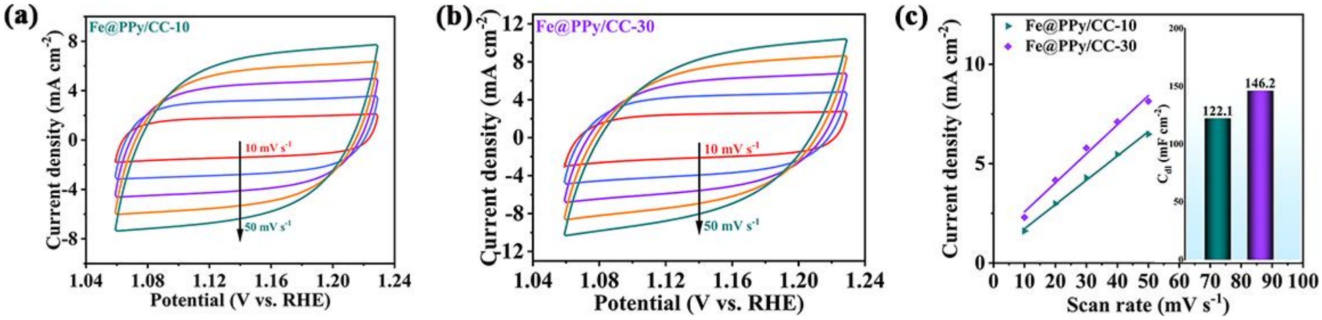

Fig. S21 CV curves of (a) Fe@PPy/CC-10 and (b) Fe@PPy/CC-30 at different scan rates of 10~50mV s^{-1}. (c) Linear plots of scan rates versus current density of Fe@PPy/CC-10 and Fe@PPy/CC-30 tested in 1.0 M KOH electrolyte.

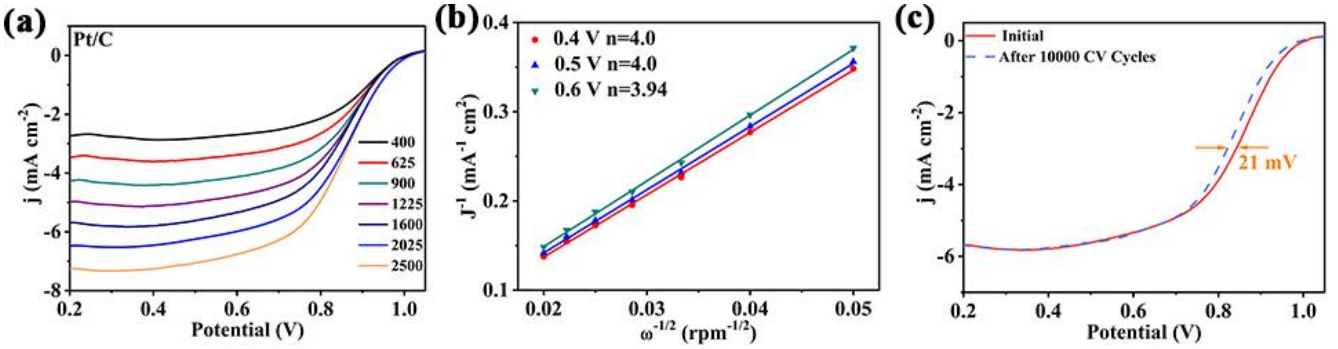

Fig. S22 ORR performance of Pt/C: (a) LSV curves of at different electrode rotating speeds from 400 to 2500 rpm. (b) The corresponding fitted K–L plots at different potentials. (c) Stability after 10000 CV cycles.

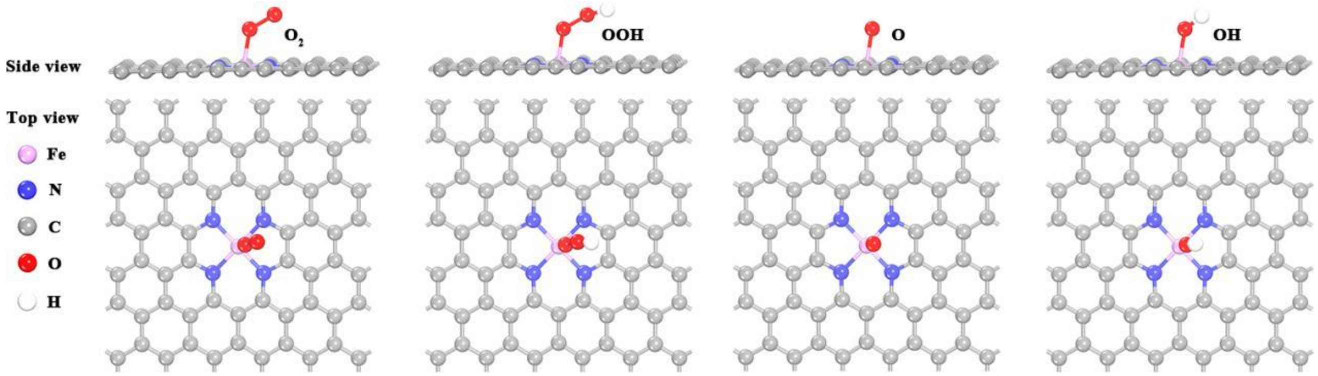

Fig. S23 DFT calculations. Side and top views of the oxygen-containing intermediates adsorbed on FeN_4 models.

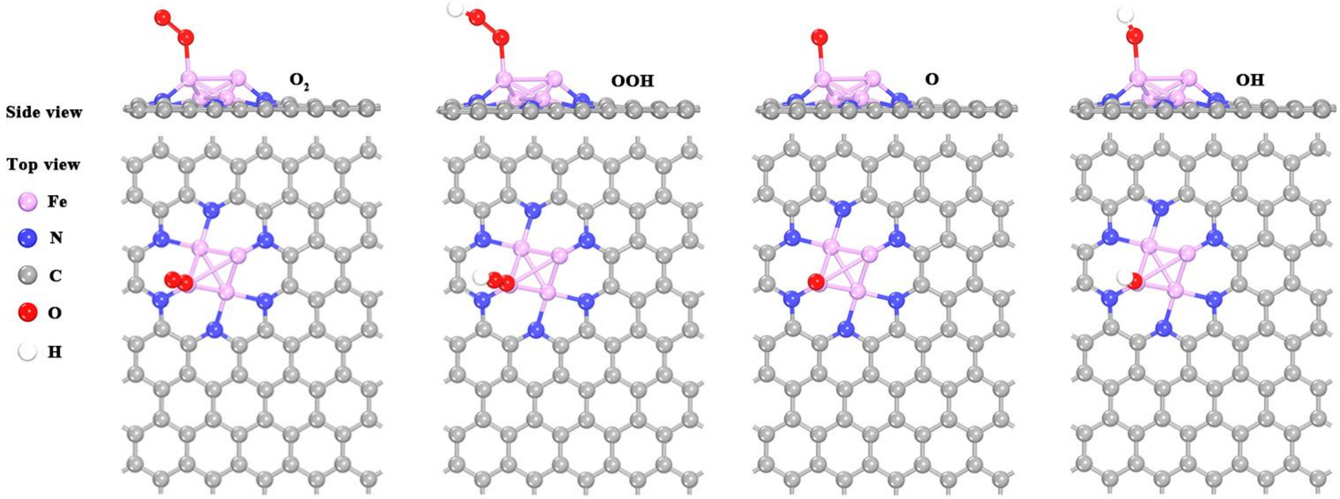

Fig. S24 DFT calculations. Side and top views of the oxygen-containing intermediates adsorbed on Fe cluster models.

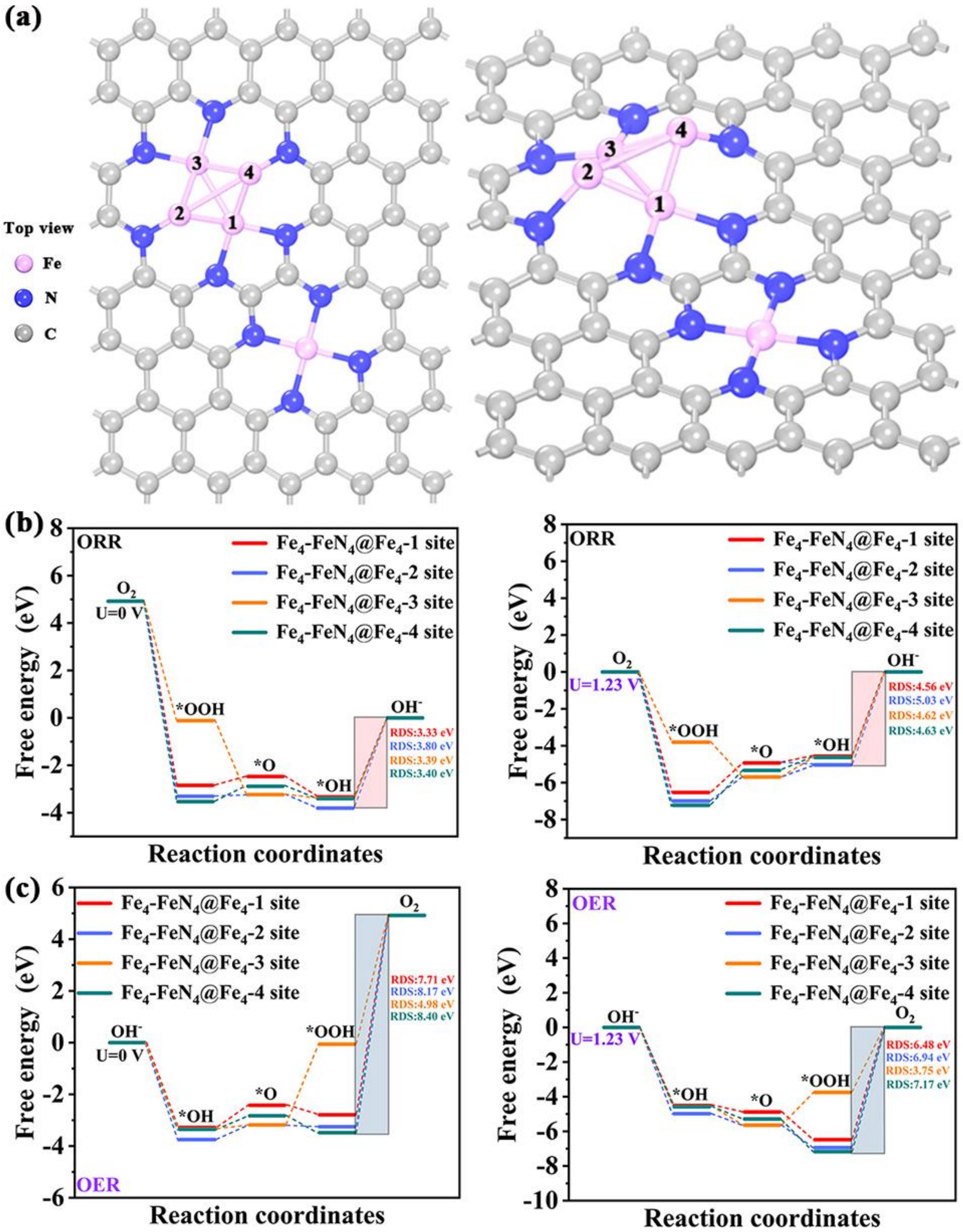

Fig. S25 (a) Top views of the Fe_4-FeN_4 models, in which the labeled 1, 2, 3 and 4 refers to the different sites on Fe cluster. Free energy diagrams of intermediate species during ORR (b) and OER (c) on different Fe sites of Fe cluster in Fe_4-FeN_4 model at U = 0 V and U = 1.23 V.

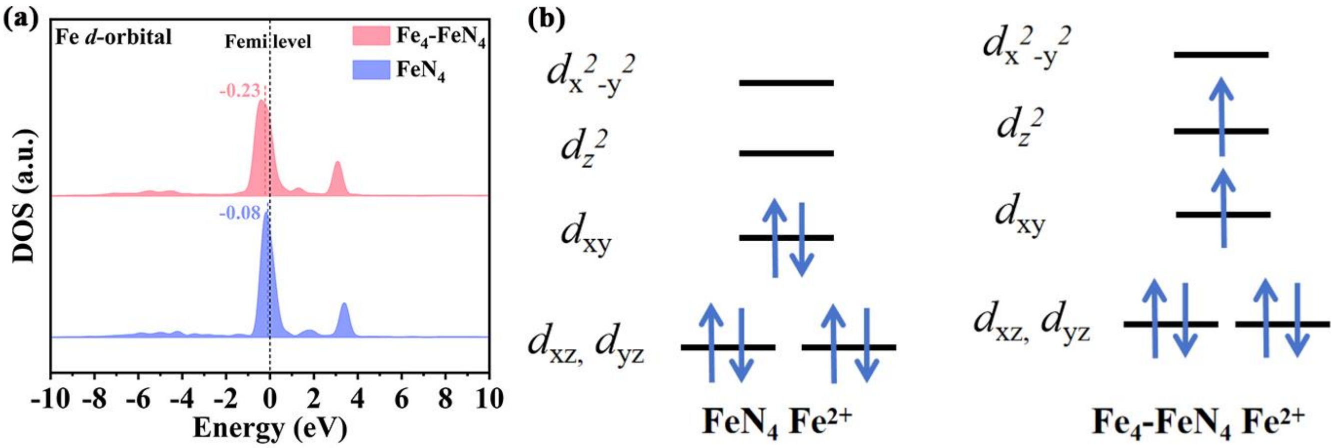

Fig. S26 (a) Fe *d*-orbital DOS of Fe_4−FeN_4 and FeN_4. (b) The electron distribution of the Fe 3*d* orbitals in Fe_4−FeN_4 and FeN_4.

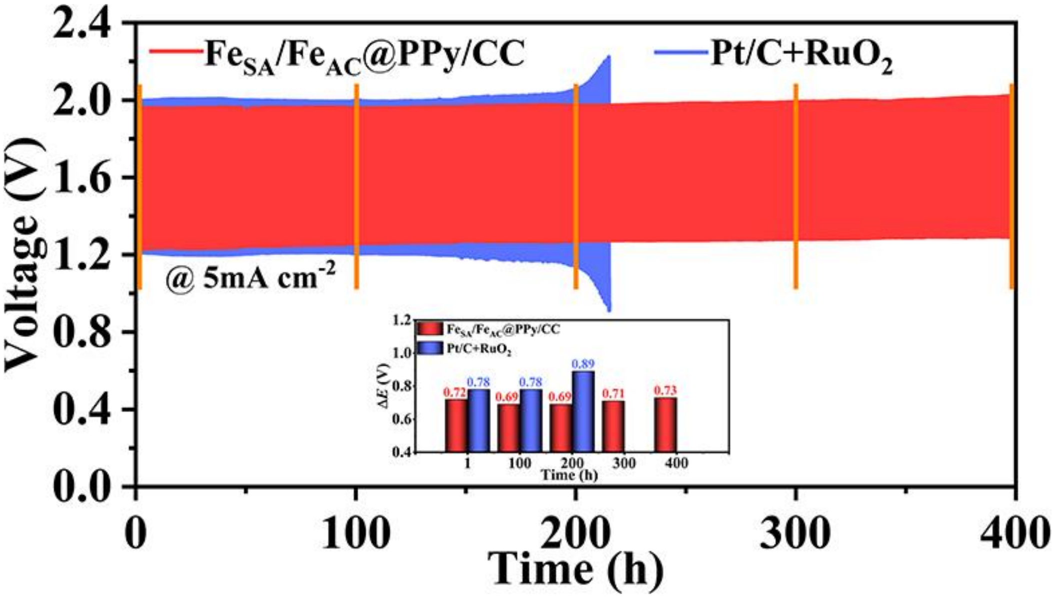

Fig. S27 Long-term galvanostatic charging–discharging plots of Fe$_{SA}$/Fe$_{AC}$@PPy/CC-based aqueous ZAB and Pt/C+RuO$_2$-based aqueous ZAB at a current density of 5 mA cm^{-2}.

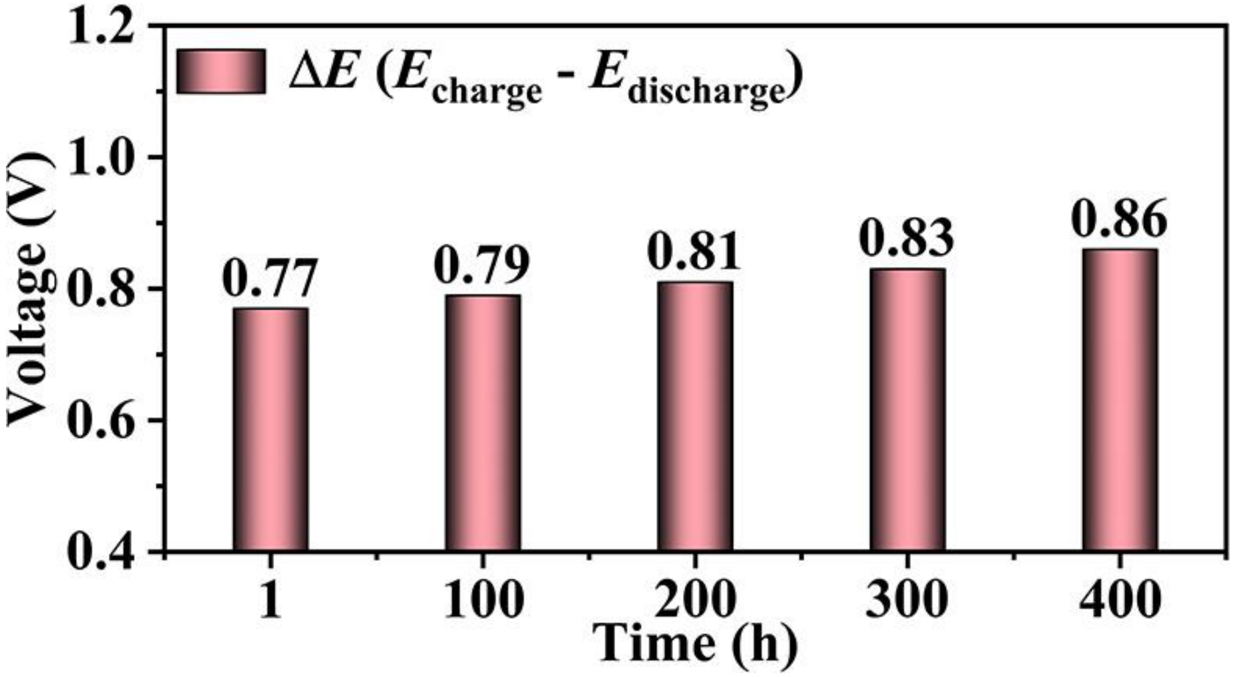

Fig. S28 The charging-discharging voltage differences of the Fe_{SA}/Fe_{AC}@PPy/CC-based aqueous ZAB at 1, 100, 200, 300, and 400 h.

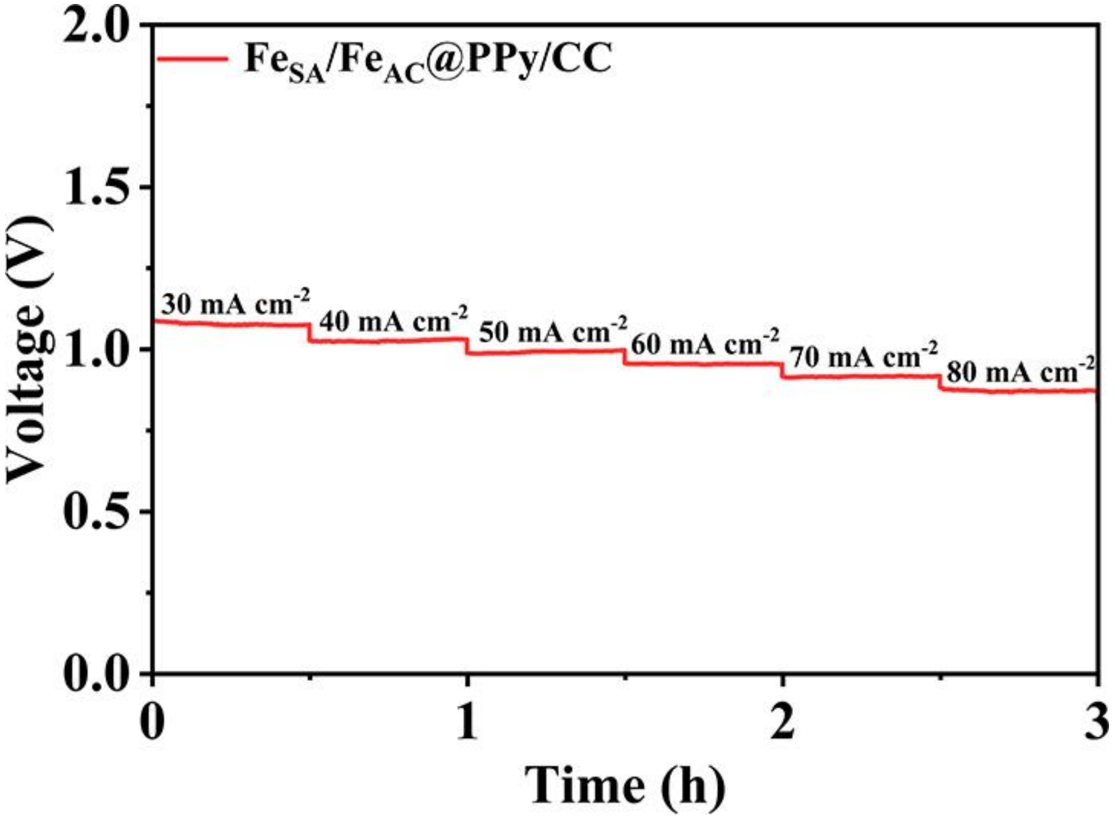

Fig. S29 Galvanostatic discharge polarization plots of the Fe$_{SA}$/Fe$_{AC}$@PPy/CC-based aqueous ZAB at 30−80 mA cm^{-2}.

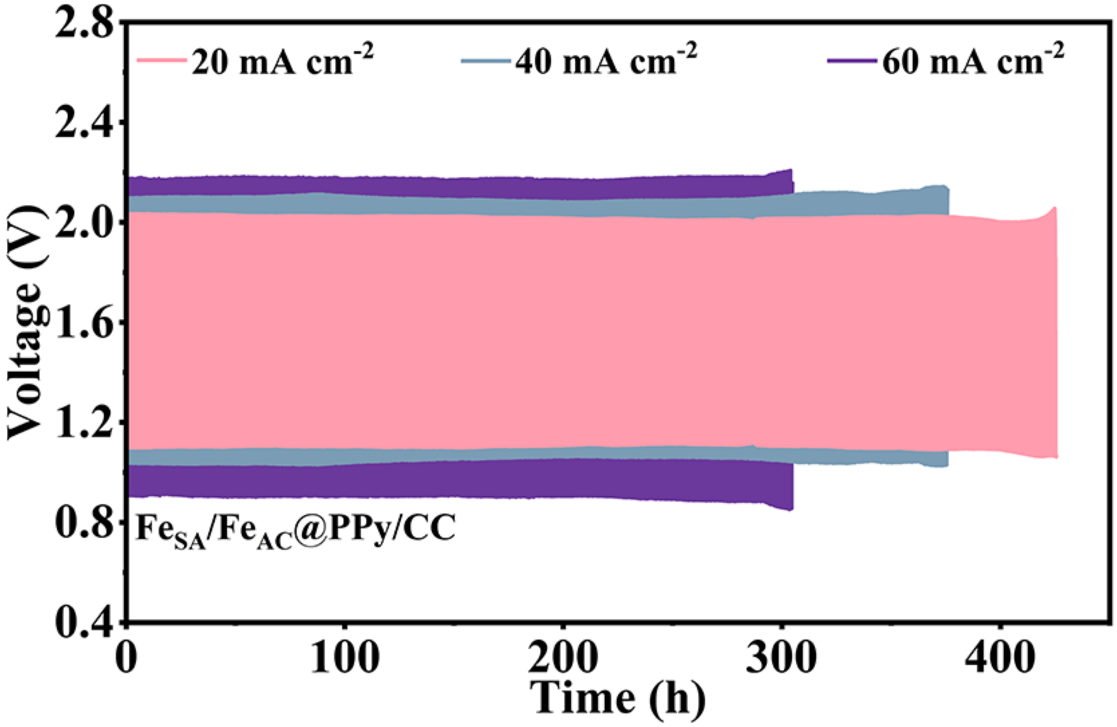

Fig. S30 Long-term galvanostatic charging-discharging curves of Fe$_{SA}$/Fe$_{AC}$@PPy/CC-based aqueous ZAB at current densities of 20 mA cm^{-2}, 40 mA cm^{-2}, and 60 mA cm^{-2}.

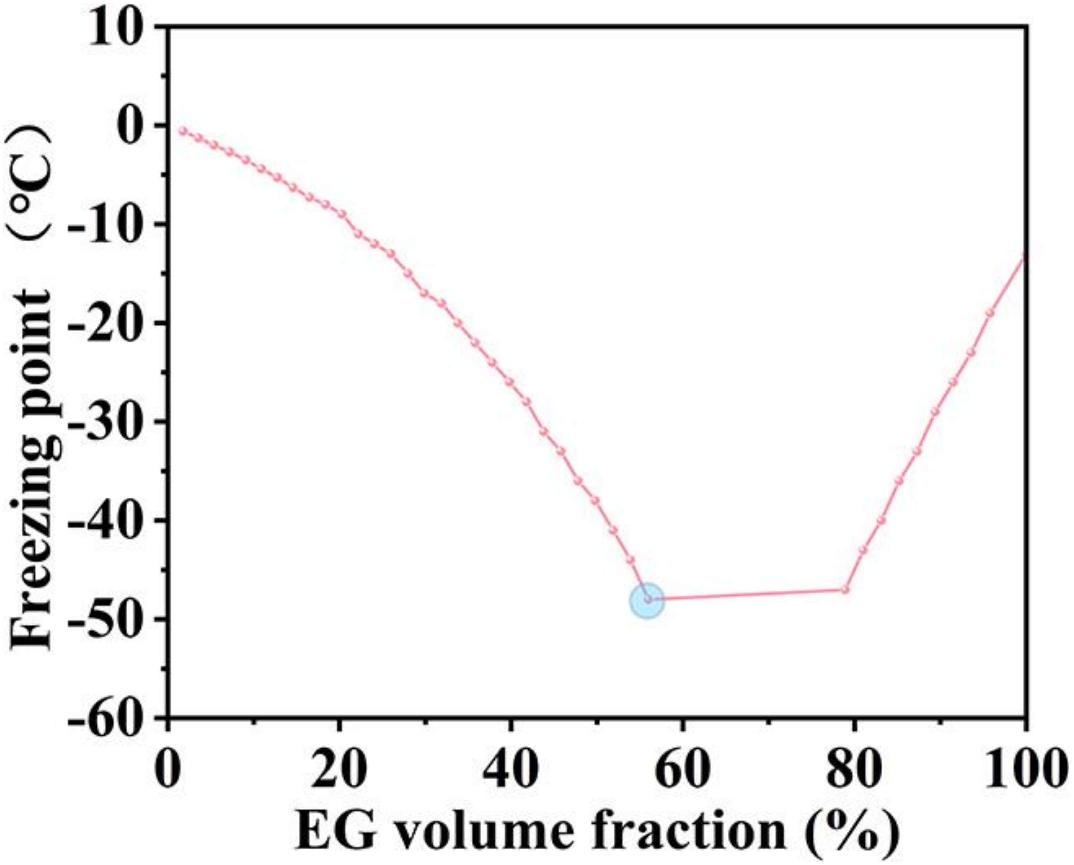

Fig. S31 The relationship between the volume fraction of EG and the freezing point.

As demonstrated in **Fig. S31**, the graph illustrating the relationship between the volume fraction of EG in aqueous solutions and the freezing point shows that the lowest freezing point is attained at a volume fraction of approximately 55% EG. Therefore, in the PAM/EG system, we incorporate an EG aqueous solution with a volume fraction of 55%.

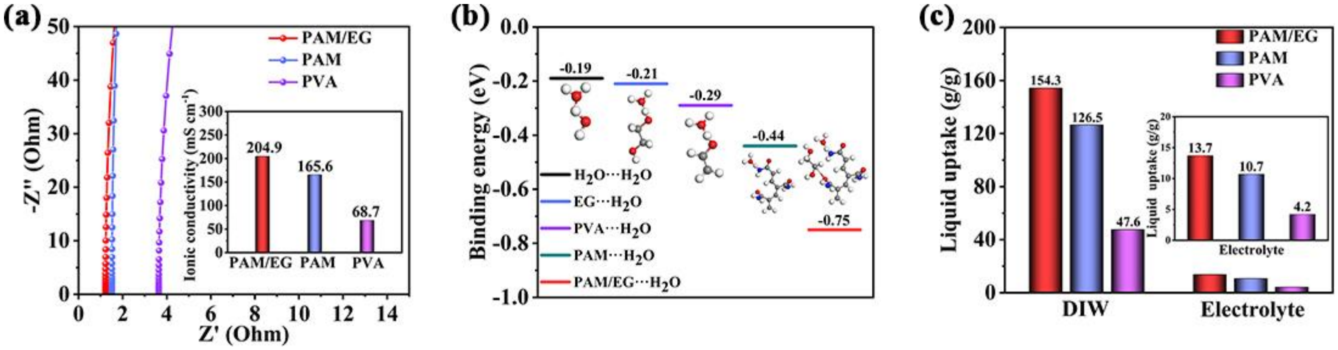

Fig. S32 (a) EIS curves and ionic conductivity performances of PAM/EG, PAM and PVA tested at 25 °C. (b) Calculated binding energies of $H_2O\cdots H_2O$, $EG\cdots H_2O$, $PVA\cdots H_2O$, $PAM\cdots H_2O$ and $PAM/EG\cdots H_2O$. (c) Liquid uptake behaviors of PAM/EG, PAM, and PVA.

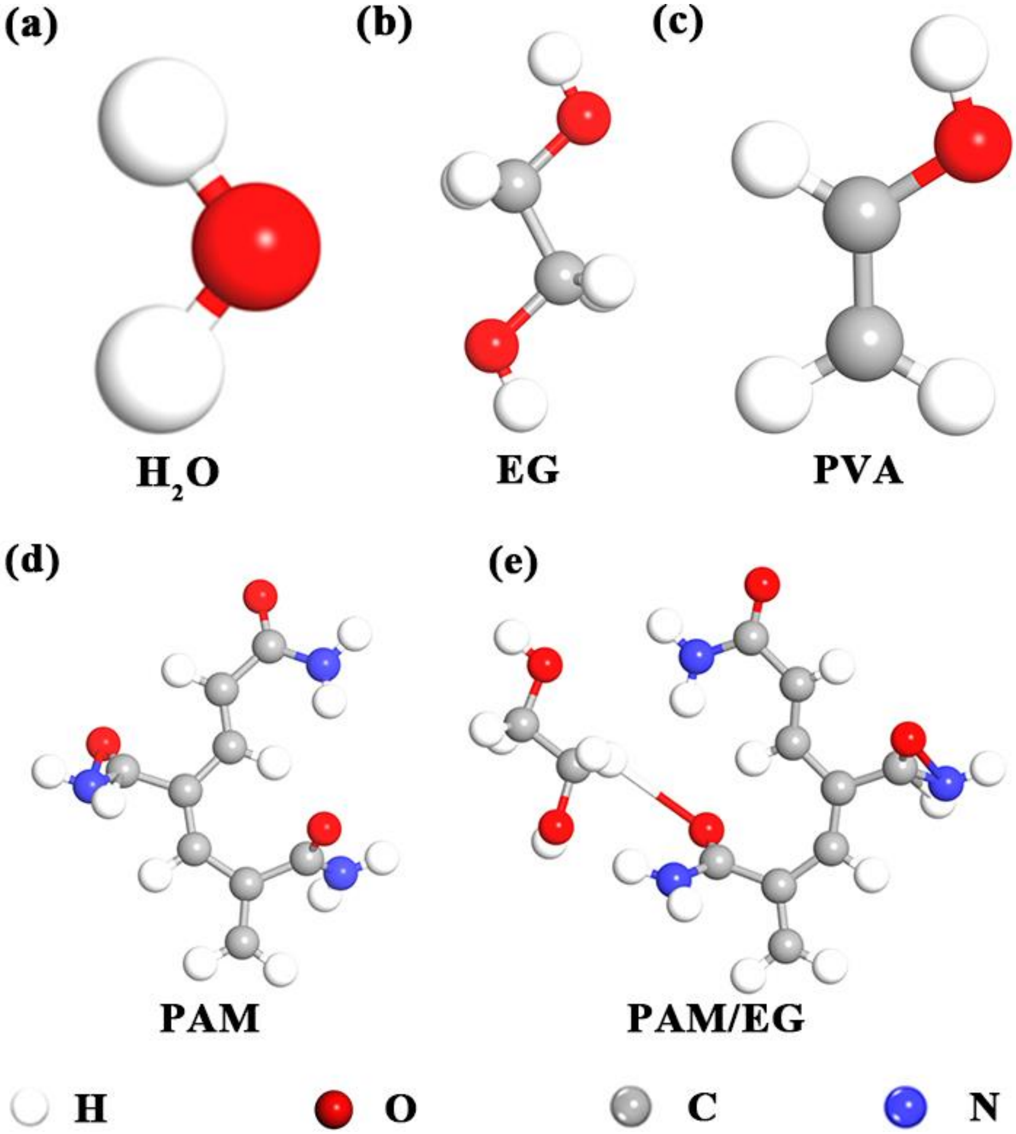

Fig. S33 DFT models: (a) H_2O, (b) EG, (c) PVA, (d) PAM and (e) PAM/EG.

DFT calculations demonstrated that the higher adsorption energy between EG with H_2O molecules (EG···H_2O) than that of between H_2O molecules (H_2O···H_2O) (−0.21 eV vs. −0.19 eV) (**Fig. S32b and S33**). It was proved that EG could form a more stable hydrogen bond network with H_2O molecules. Furthermore, the adsorption energy of PAM/EG···H_2O was approximately 1.7 times as that of PAM···H_2O (−0.44 eV) and 2.9 times as that of PVA···H_2O (−0.29 eV). It implied that the introduction of EG significantly promoted the interaction force of PAM with H_2O molecules, forming a stronger intermolecular hydrogen bond network. It was concluded that the energy required to overcome intermolecular forces for H_2O loss and freezing increased. Therefore, from a theoretical perspective, PAM/EG is expected to demonstrate superior water retention capabilities and an extensive operational temperature range.

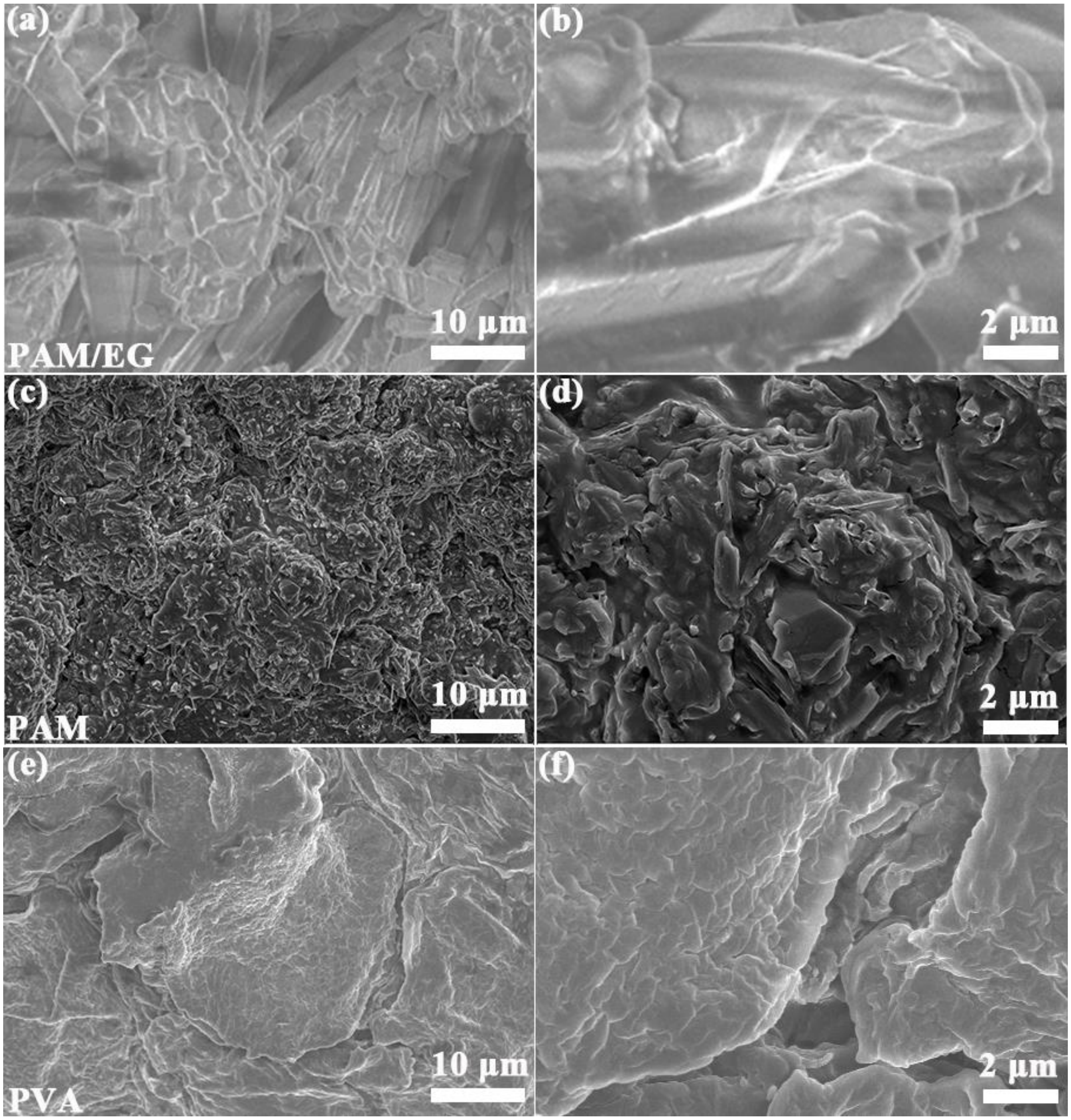

Fig. S34 SEM images of (a,b) PAM/EG, (c,d) PAM, and (e,f) PVA after freeze-drying.

As the SEM images shown in **Fig. S34a,b**, the needle-like structures of PAM/EG could produce a certain level of porosity between the molecules. In contrast, both PAM and PVA display block-like structures with no apparent porosity on the surfaces (**Fig. S34c-f**). It indicated that the porous structure of PAM/EG contributed to the enhanced ability of GPEs to store electrolyte solutions and retain moisture. Water retention capability is a critical parameter indicator for GPEs. As depicted in **Fig. 6b**, PVA exhibited the most rapid loss of water with a dehydration rate of 22.6 % in just one day. Such rapid loss is primarily due to the swift evaporation of free H_2O molecules within the electrolyte. Conversely, PVA/EG exhibited superior water retention capabilities with a 75.4 % retention even after seven days.

This phenomenon can be attributed to the high density of intermolecular −OH groups in EG, which enhances the interaction between the electrolyte and H_2O molecules, thereby reducing the loss of free H_2O molecules.

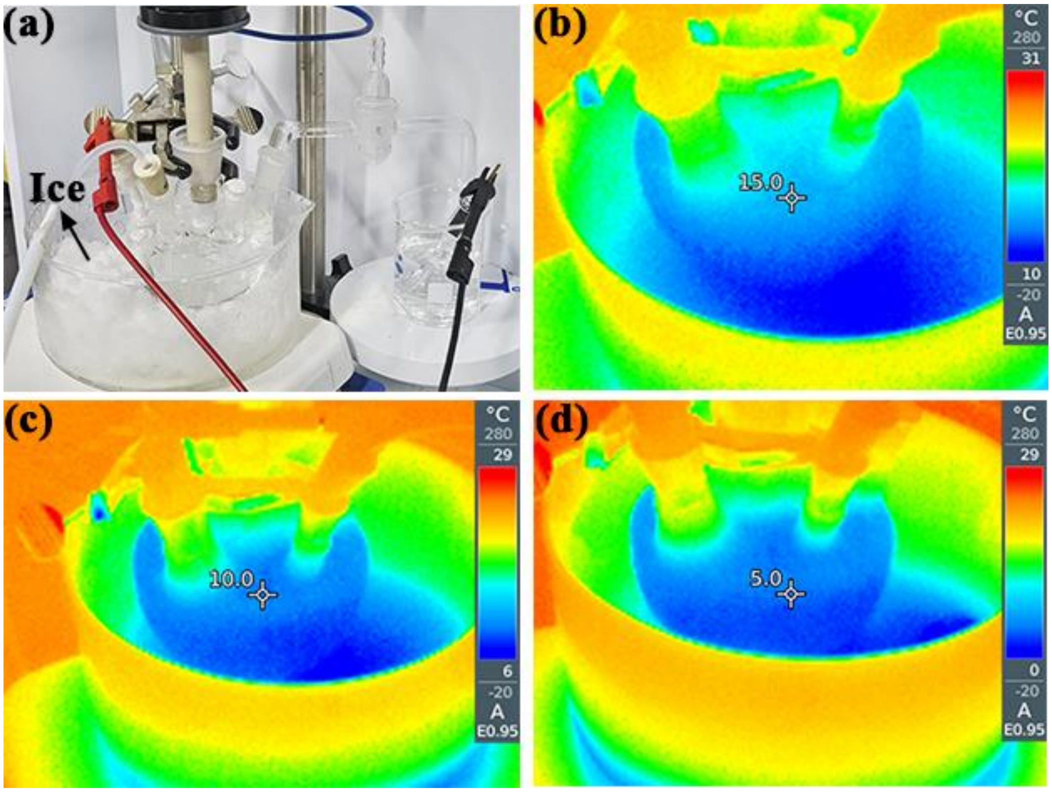

Fig. S35 (a) ORR test apparatus at low-temperature. Real-time infrared thermal sensitivity images of (b) 15 ℃, (c) 10 ℃, and (d) 5 ℃.

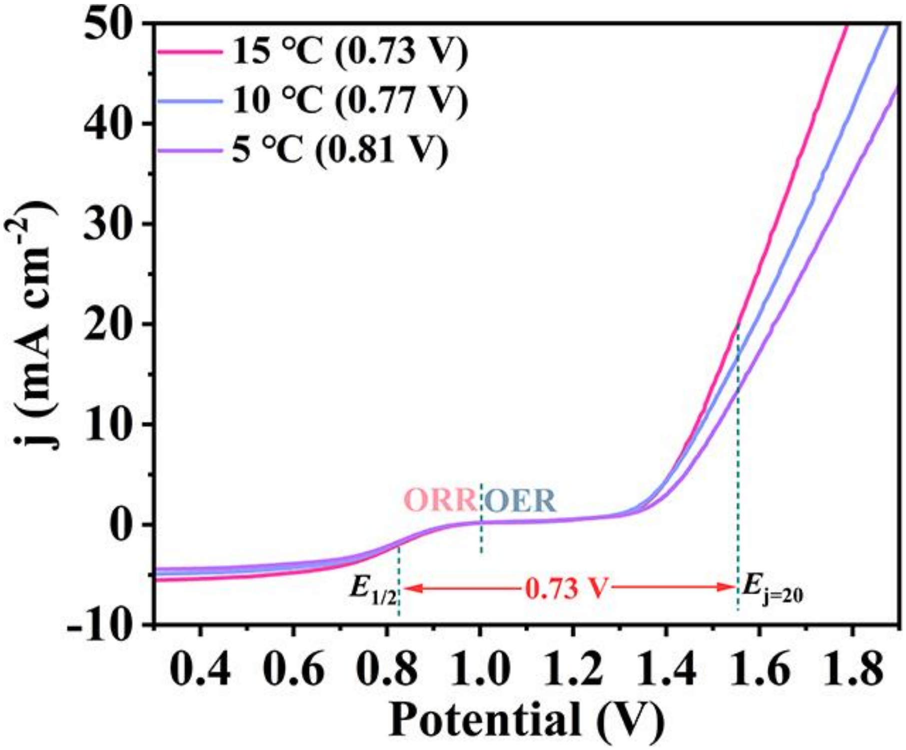

Fig. S36 LSV curves of Fe_{SA}/Fe_{AC}@PPy/CC in the OER and ORR regions tested in O_2-saturated 0.1 M KOH at low temperatures of 15 °C, 10 °C and 5 °C.

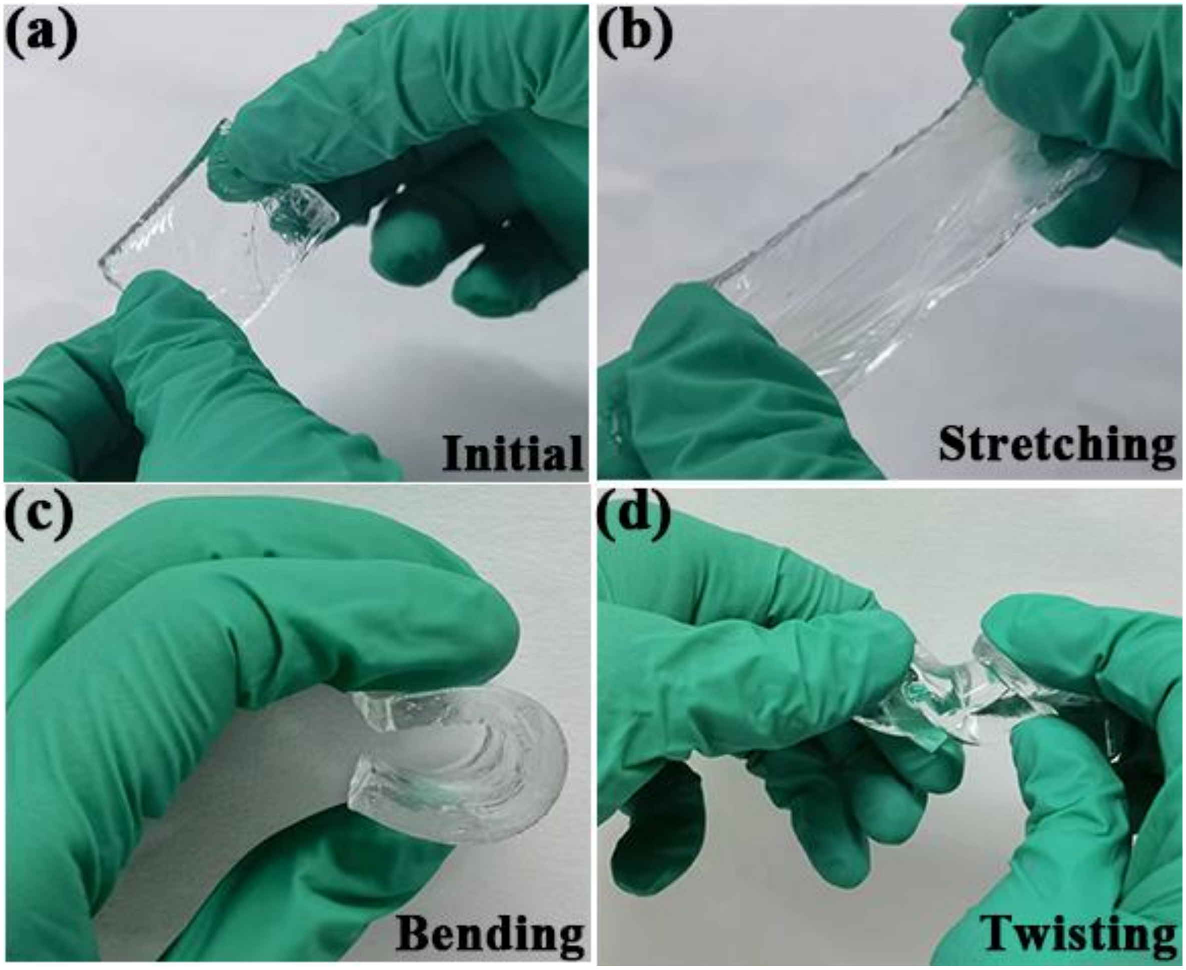

Fig. S37 Photos of (a) initial, (b) stretching, (c) bending and (d) twisting capability for PAM/EG GPE.

As illustrated in **Fig. S37**, PAM/EG GPE was subjected to arbitrary stretching, bending, and twisting without any surface fracturing, proving its potential for real-world applications under extreme mechanical conditions. It demonstrated the superior mechanical performance and stability of PAM/EG GPE.

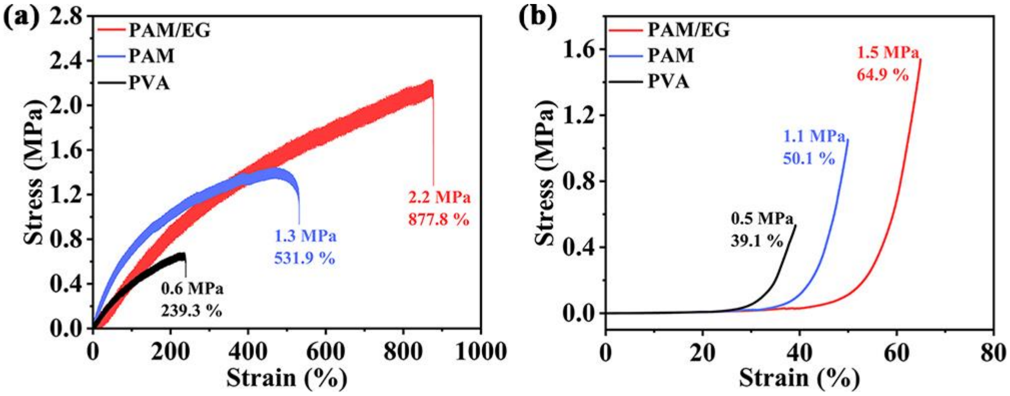

Fig. S38 (a) Tensile and (b) compression tests of PAM/EG, PAM and PVA GPEs.

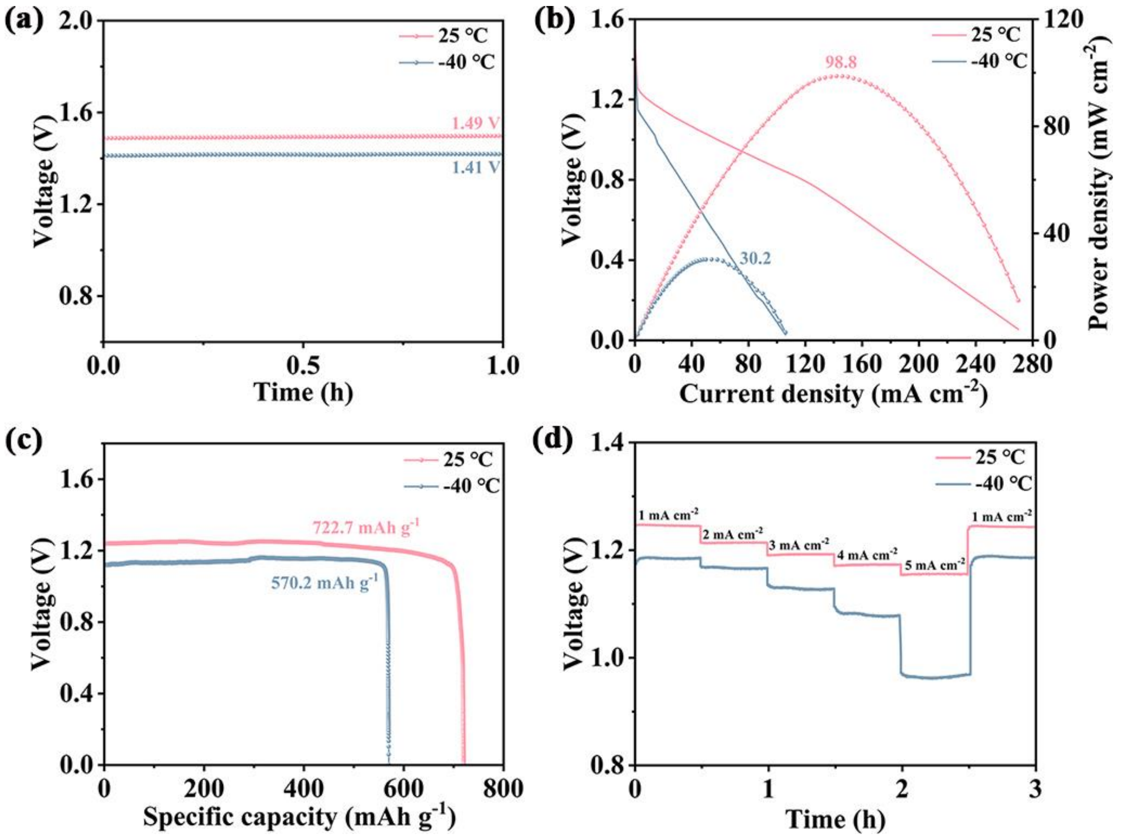

Fig. S39 (a) Open-circuit voltages, (b) discharging curves and the corresponding power density plots, (c) specific discharging capacities at 2 mA cm^{-2} and (d) rate performance of Fe$_{SA}$/Fe$_{AC}$@PPy/CC-based FZABs by using PAM/EG GPE as the electrolyte at 25 ℃ and −40 ℃.

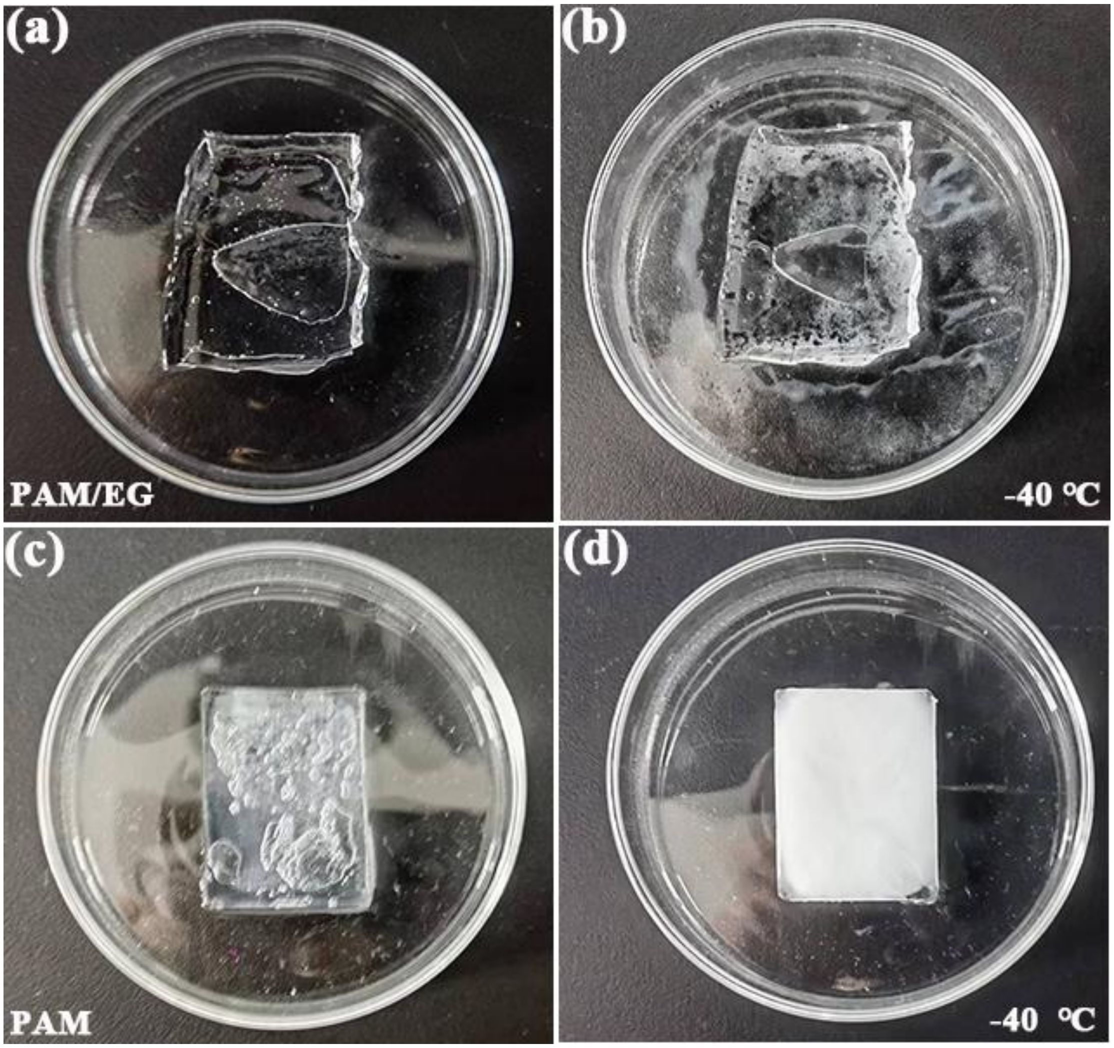

Fig. S40 Photos of (a, b) PAM/EG GPE and (c, d) PAM GPE freezing at –40 °C.

As shown in **Fig. S40**, the surface of PAM/EG did not exhibit noticeable ice crystal formation at the low temperature of −40 °C, whereas the pure PAM obviously froze due to its inferior low-temperature resistance.

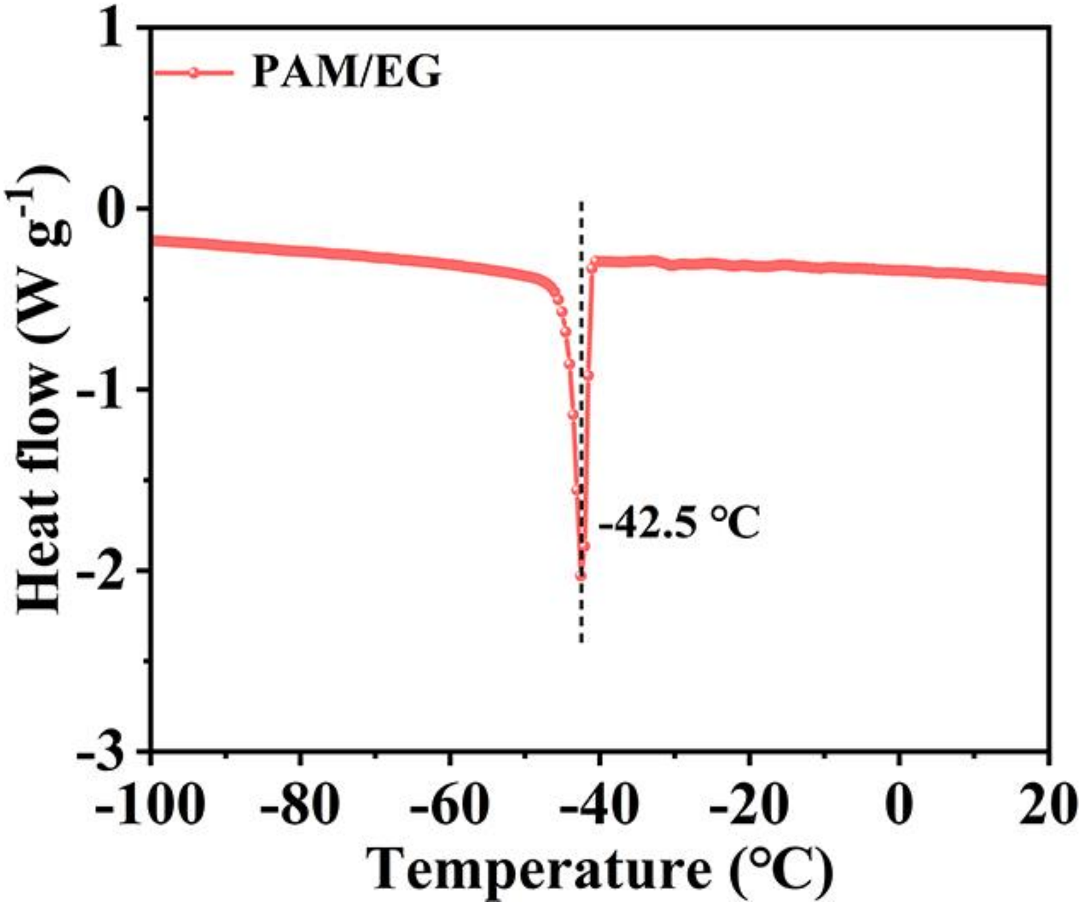

Fig. S41 DSC curve of PAM/EG GPE recorded at temperature window range from −100 °C to 20 °C.

Differential scanning calorimetry (DSC) measurements were conducted to investigate the operational temperatures of the PAM/EG. As shown in **Fig. S41**, the thermal transition peak of PAM/EG occurs at −42.5 °C, further demonstrating its exceptional resistance to low temperatures.

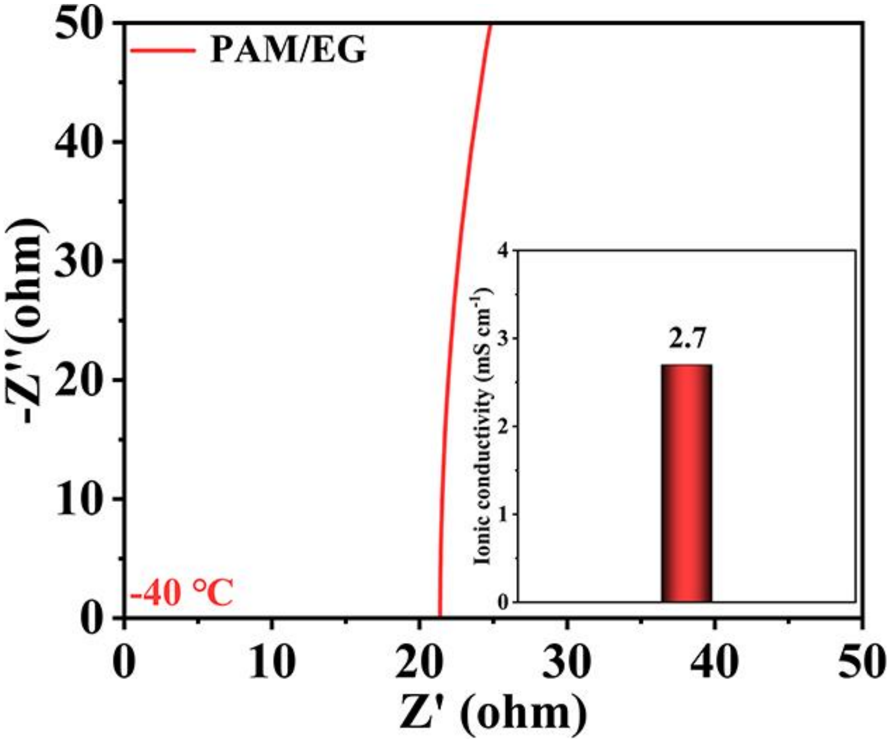

Fig. S42 EIS curve and ionic conductivity of PAM/EG tested at −40 ℃.

To further investigate the low-temperature mass transfer properties of PAM/EG at −40 °C, EIS tests were conducted and the ionic conductivity was calculated. As illustrated in **Fig. S42**, PAM/EG exhibits an ionic conductivity of 2.7 mS cm^{-1} at −40 °C, demonstrating its robust mass transfer capability. It suggests that PAM/EG can effectively function as an electrolyte medium for zinc anodes and air cathodes in FZABs under low-temperature conditions.

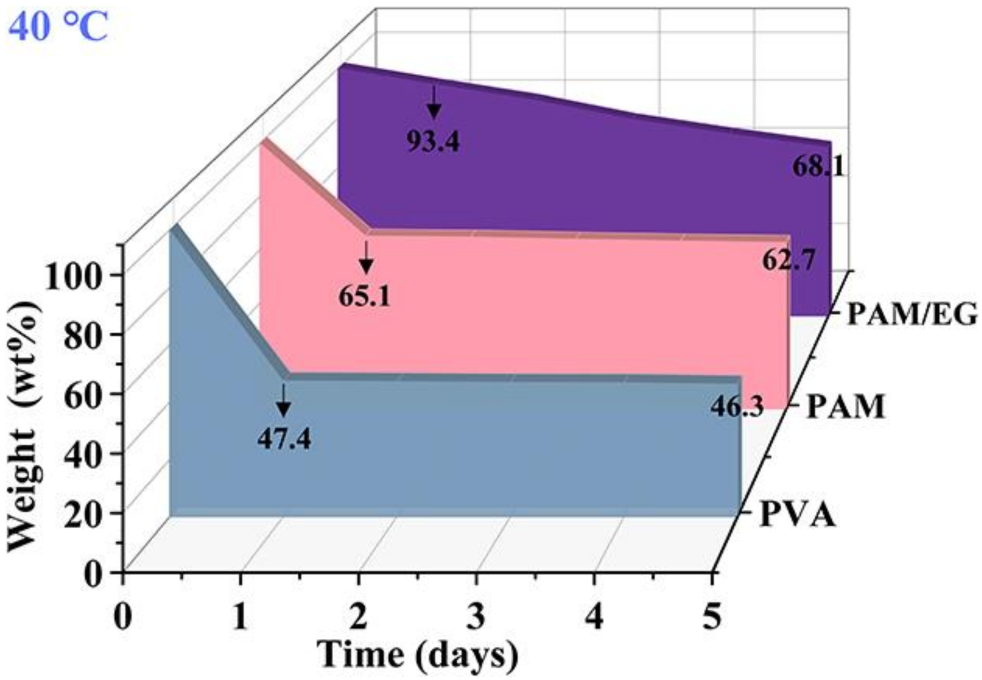

Fig. S43 Liquid retention capability of PAM/EG, PAM and PVA at 40 ℃.

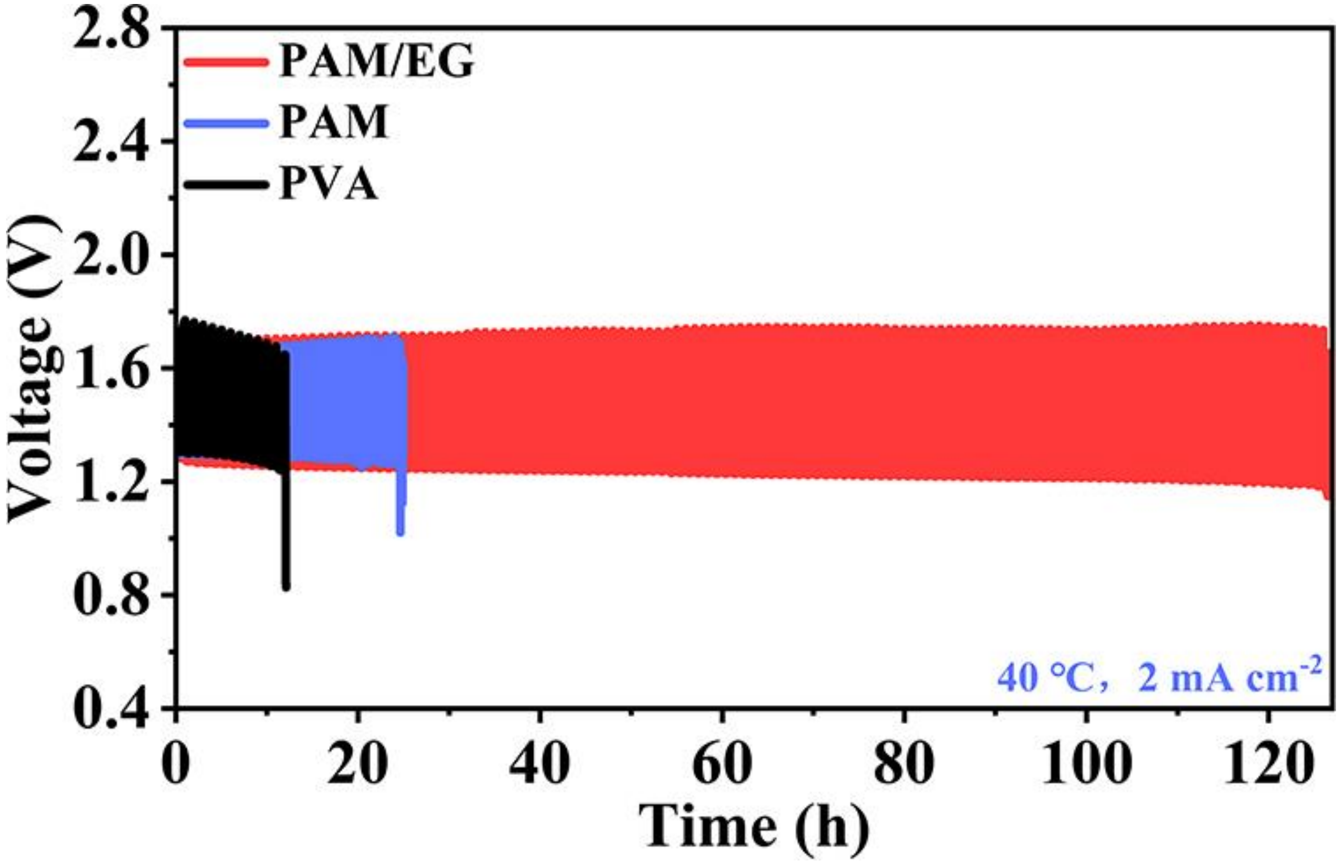

Fig. S44 Galvanostatic cycling curves with 30 min discharging and 30 min charging per cycle under 40 °C at 2 mA cm^{-2}.

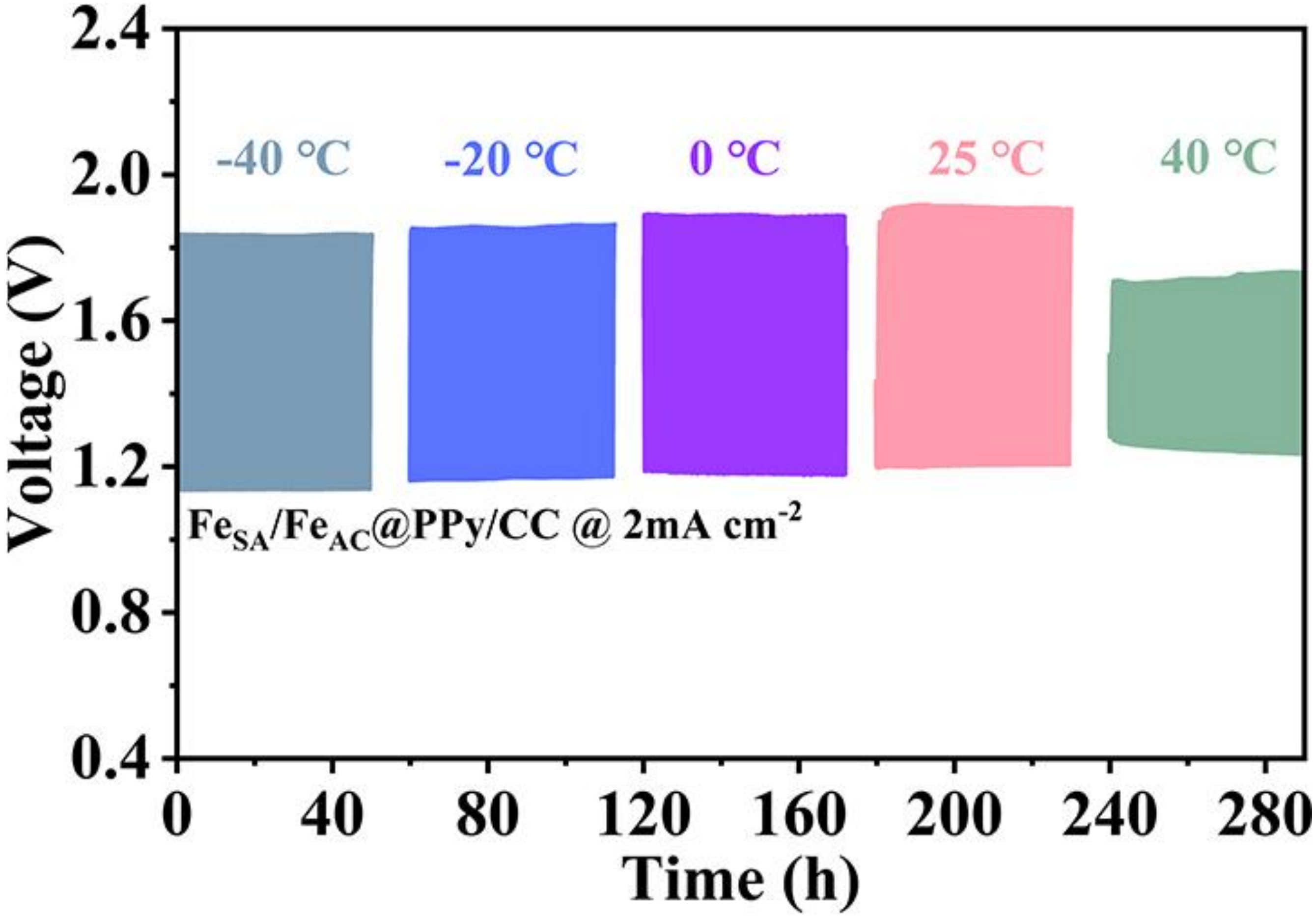

Fig. S45 long-time discharge-charge cycling curves of sandwich-type FZAB with PAM/EG electrolyte and Fe$_{SA}$/Fe$_{AC}$@PPy/CC catalyst under different temperatures. Each cycle involved charging and discharging for a duration of 1 h, conducted over a total of 50 h at each temperature.

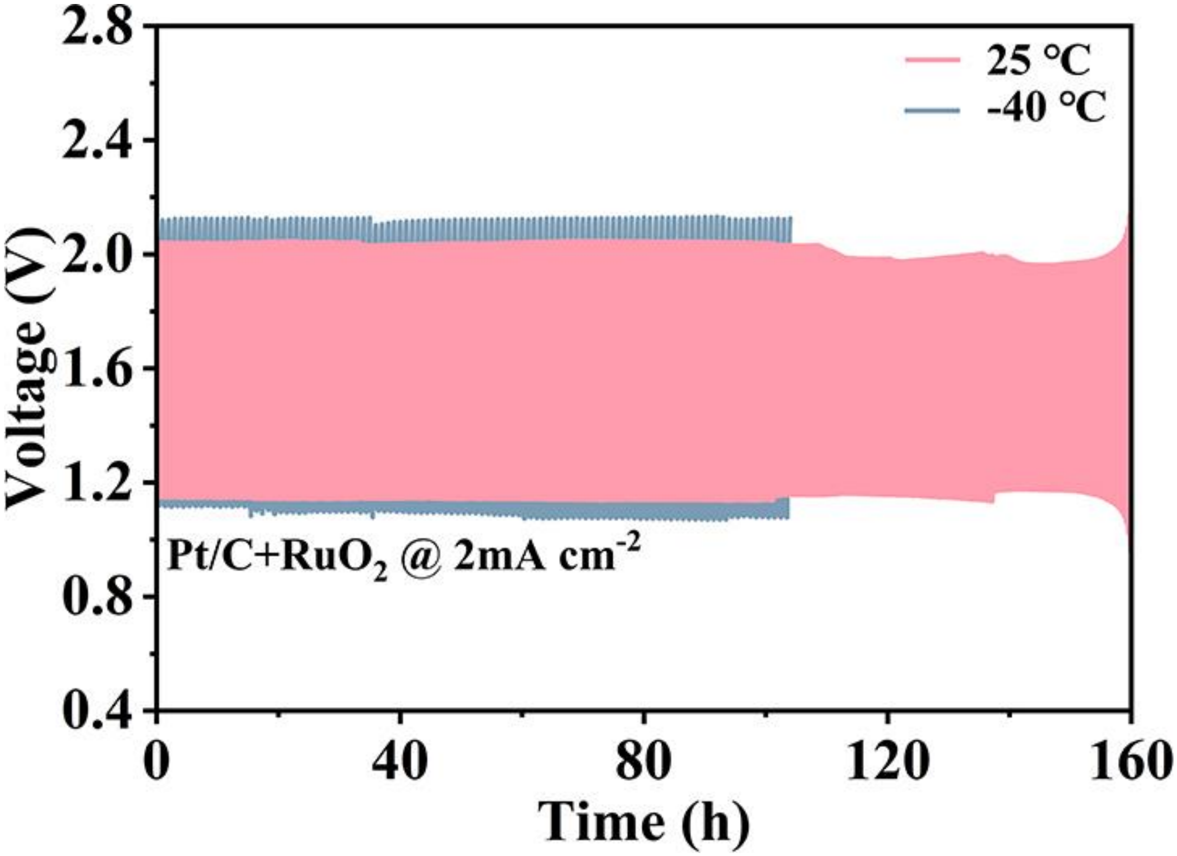

Fig. S46 Galvanostatic cycling curves with 30 min discharging and 30 min charging per cycle of the Pt/C+RuO$_2$-based FZAB at 25 °C and −40 °C.

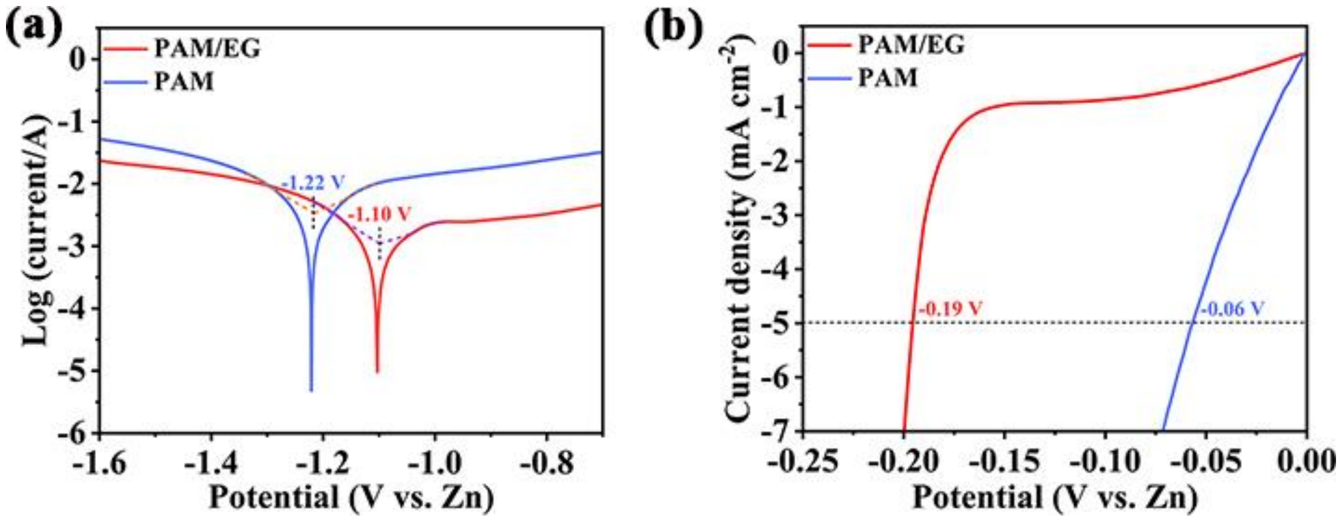

Fig. S47 (a) Corrosion rate curves of zinc anode and (b) HER polarization curves in PAM/EG and PAM electrolytes.

Table S1. The Fe content for different samples tested by ICP-OES.

Samples	**Content (wt%)**
Fe@PPy/CC-10	0.56
Fe_{SA}/Fe_{AC}@PPy/CC	0.92
Fe@PPy/CC-30	1.22

Table S2. Structural parameters of Fe_{SA}/Fe_{AC}@PPy/CC, Post-OER of Fe_{SA}/Fe_{AC}@PPy/CC, Fe@PPy/CC-10, Fe@PPy/CC-30, Fe_{SA}/Fe_{AC}@PPy/CC-0.8, Fe_{SA}/Fe_{AC}@PPy/CC-1.0 and Fe foil determined from the FT-EXAFS spectra fitting.

Samples	**Path**	**CN**	**R (Å)**	**ΔE_0 (eV)**	**σ^2(10^{-3}Å^2)**	**R-factor**
Fe_{SA}/Fe_{AC}@PPy/CC	Fe−N	3.78	2.07	2.43	0.0064	0.011
	Fe−Fe	2.76	3.17	9.28	0.0095	
Post-OER of Fe_{SA}/Fe_{AC}@PPy/CC	Fe−N	3.57	2.04	1.65	0.0039	0.007
	Fe−Fe	2.58	3.06	1.65	0.0054	
Fe@PPy/CC-10	Fe−N	5.88	2.08	2.24	0.0081	0.007
	Fe−Fe 1	1.90	2.40	2.24	0.0034	
	Fe−Fe 2	2.15	2.61	−1.06	0.0042	
Fe@PPy/CC-30	Fe−N	3.69	2.03	−3.42	0.0057	0.011
	Fe−Fe 1	8.66	2.60	12.34	0.0081	
	Fe−Fe 2	7.37	2.75	2.08	0.0065	
Fe_{SA}/Fe_{AC}@PPy/CC-0.8	Fe−N	3.00	1.99	−2.69	0.0059	0.001
	Fe−Fe	9.71	2.97	−3.17	0.0374	
Fe_{SA}/Fe_{AC}@PPy/CC-1.0	Fe−N	3.71	2.03	−0.02	0.0084	0.006
	Fe−Fe	5.60	3.08	3.95	0.0331	
Fe foil	Fe−Fe 1	8.00	2.47	6.23	0.0067	0.007
	Fe−Fe 2	6.00	2.83	5.72	0.0075	

Note: *CN*, coordination number; *R*, the distance to the neighboring atom; σ^2, the Mean Square Relative Displacement (MSRD); ΔE_0, inner potential correction; All the *R*-factors for the fitted results are within 0.02, indicating the goodness of the fitting.

Table S3. Structural parameters of the samples prepared through constant potential deposition of iron species on PPy/CC substrates at different potentials for 10 min from the FT-EXAFS spectra fitting as shown in Fig. S7(c-j).

Potential	Path	CN	R (Å)	ΔE_0 (eV)	$\sigma^2(10^{-3}Å^2)$	R-factor
0.2 V	Fe−N	2.52	1.99	3.72	0.0072	0.009
0.1 V	Fe−N	3.86	2.00	−0.44	0.0092	0.019
−0.2 V	Fe−N	4.09	1.92	−3.94	0.0062	0.018
	Fe−Fe	1.14	2.45	−3.94	0.0086	
−0.3 V	Fe−N	7.38	2.04	3.34	0.0014	0.008
	Fe−Fe	0.79	2.51	−2.77	0.0018	
−0.4 V	Fe−N	3.05	2.04	−7.42	0.0184	0.007
	Fe−Fe	0.96	2.97	−1.37	0.0096	
−0.5 V	Fe−N	2.37	2.02	−1.75	0.0026	0.006
	Fe−Fe	0.64	2.49	−2.40	0.0007	
−0.6 V	Fe−N	3.77	2.05	2.02	0.0100	0.019
	Fe−Fe	1.24	2.68	−7.25	0.0023	

Note: *CN*, coordination number; *R*, the distance to the neighboring atom; σ^2, the Mean Square Relative Displacement (MSRD); ΔE_0, inner potential correction; All the *R*-factors for the fitted results are within 0.02, indicating the goodness of the fitting.

Table S4. Content of different N-type calculated from the N 1s spectra of Fe@PPy/CC-10, Fe_{SA}/Fe_{AC}@PPy/CC, and Fe@PPy/CC-30.

Samples	Pyridinic−N (%)	Fe−N (%)	Graphitic−N (%)	Oxidized N (%)
Fe@PPy/CC-10	57.05	35.10	5.61	2.24
Fe_{SA}/Fe_{AC}@PPy/CC	61.09	16.12	18.78	4.01
Fe@PPy/CC-30	41.75	28.13	15.82	14.30

Table S5. The contents and proportions of Fe single atoms and Fe clusters in Fe@PPy/CC-10, Fe_{SA}/Fe_{AC}@PPy/CC, and Fe@PPy/CC-30 were calculated by fitting the FT-EXAFS spectra.

Samples	**Fe single atom content (wt%)**	**Fe cluster content (wt%)**	**Ratio**
Fe@PPy/CC-10	0.298	0.262	1.14:1
Fe_{SA}/Fe_{AC}@PPy/CC	0.184	0.736	1:4
Fe@PPy/CC-30	0.624	0.596	1.05:1

Table S6. Performance comparison of ORR, OER and aqueous ZABs assembled by Fe_{SA}/Fe_{AC}@PPy/CC as the air-cathode and other reported atomic dispersion catalysts.

Catalysts	ORR $E_{1/2}$ (V)	OER E (V) @ j (mA cm^{-2})	ΔE (V)	Max power density (mW cm^{-2})	Current density (mA cm^{-2})	Charge/discharge voltage gap (V)	Cyclic time (h)	References
Fe_{SA}/Fe_{AC}@PPy/CC	0.83	1.524@20	0.694	205.3	10	0.79	300	This work
SA-Fe-SNC@900	0.876	1.632@10	0.756	218.6	10	0.80	120	[3]
FeSNC-TA	0.91	1.70@10	0.79	85.6	5	~0.96	300	[4]
FeCoNC/B	0.892	1.592@10	0.70	157	10	0.70	40	[5]
Arc-Co SAC	0.86	1.58@10	0.72	96.4	2	~0.54	20	[6]
FeN_4/G/FeCo	0.90	1.55@10	0.65	197.2	3	~0.83	165	[7]
CoSAs@NC-920	0.882	1.590@10	0.708	166	2	0.791	155	[8]
AC-CuFe-NC	0.92	1.57@10	0.65	195.8	7.8	0.81	125	[9]
Fe–N–C-2	0.83	1.687@10	0.857	71.6	10	~0.82	30	[10]
ZnCoFe–N–C	0.878	1.598@10	0.720	137.8	2	0.81	90	[11]
$FeNi_{jns}$/NC	0.92	1.67@10	0.75	/	10	1.14	140	[12]
ZIF8@FePMPDA-920	0.90	1.53@10	0.63	123.11	5	0.79	140	[13]
COPBTC-Co	0.864	1.627@10	0.763	157.7	10	~0.80	100	[14]
Fe–N@Ni–HCFs	0.88	1.567@10	0.687	172.2	10	0.70	200	[15]
NP-Co_{SA}NC	0.86	1.55@10	0.69	158.1	10	0.88	80	[16]
Cu-Se DAs	0.905	1.655@10	0.750	/	10	~1.2	70	[17]

Table S7. The entropy and zero−point energy corrections values.

Species	H_2O	H_2	*OH	*OOH	*O
T*S (eV) (298K)	0.67	0.40	0.01	0	0
ZPE (eV)	0.56	0.27	0.31	0.35	0.05

Table S8. The calculated adsorption energies of O_2 on Fe_4–FeN_4, FeN_4 and Fe cluster models.

Models	$\boldsymbol{E}_{\mathbf{O2/surface}}$ **(eV)**	$\boldsymbol{E}_{\mathbf{O2}}$ **(eV)**	$\boldsymbol{E}_{\mathbf{surface}}$ **(eV)**	$\Delta\boldsymbol{E}_{\mathbf{*O2}}$ **(eV)**
Fe_4–FeN_4	–17510.09	–867.98	–16637.54	–4.57
FeN_4	–11192.73	–867.98	–10320.46	–4.29
Fe cluster	–16496.93	–867.98	–15620.38	–8.57

Table S9. Performance comparison of Fe_{SA}/Fe_{AC}@PPy/CC-based FZABs with other atomic dispersion catalysts-based FZABs at room temperature and low temperature condition.

Catalysts	**GPEs**	**T (°C)**	**Current density (mA cm^{-2})**	**Cyclic time (h)**	**T (°C)**	**Current density (mA cm^{-2})**	**Cyclic time (h)**	**References**
Fe_{SA}/Fe_{AC}@PPy/CC	PAM/EG	25	2	210	–40	2	167	This work
ZnCoFe–N–C	PANa	25	2	32	/	/	/	[11]
ZIF8@FePMPDA-920	PAA film	25	1	32	/	/	/	[13]
FeMn-DSAC	PAM/MMT	25	2	80	–40	2	29	[18]
Co SA-NDGs	PAM organohydrogel	25	2	200	–40	0.5	400	[19]
Fe_x/FeN_3S_1–C	CNF@PVA-SSE	25	5	150	–40	0.5	115	[20]
FeMn-N/S-C-1000	PAA	25	10	96	–40	2	170	[21]
Fe-NNC_V	PVA	25	5	9.5	/	/	/	[22]
$Co_{SAs\text{-}NPs}$/NC	Alkaline gel	25	1	110	/	/	/	[23]
FeCo-NPC BAH	Alkalified PAA	/	/	/	–20	5	100	[24]
Co-SAs/N–C/rGO	PAA gel	25	1	26.3	/	/	/	[25]

Table S10. Performance comparison of Fe_{SA}/Fe_{AC}@PPy/CC-based FZABs with other catalysts at room temperature and low temperature condition.

Catalysts	**GPEs**	**T (°C)**	**Current density (mA cm^{-2})**	**Cyclic time (h)**	**T (°C)**	**Current density (mA cm^{-2})**	**Cyclic time (h)**	**References**
Fe_{SA}/Fe_{AC}@PPy/CC	PAM/EG	25	2	210	–40	2	167	This work
V-CMO/rGO	PAA	25	2	28	–40	2	82	[26]
Pt_1-FeO_x/CN	PAM	/	/	/	–40	2	120	[27]
Pt/RuO_2/CC	PAM-CNF/KOH/KI	20	2	40	–40	2	75	[28]
FeCo–P/N–C–F	(A-PAA)-W	25	2	92	–30	2	92	[29]
CO_3O_4/RuO_2	OHE	25	1	59	–40	1	45	[30]
CMN-231H	PAMC	/	/	/	–20	5	3.5	[31]
$(Co,Fe)_3O_4$	GPE-KOH-KI	21	2	100	–28	2	100	[32]
CoFe/AC	PAM-SC	25	0.5	42	–40	0.5	70	[33]
S–LDH/NG	PVA gel	25	5	16.7	/	/	/	[34]
NiO/CoO TINWs	PVA gel	25	1	33	–10	1	14	[35]
SV-900	C20E2G5 gel	20	2	50	–40	2	50	[36]

References:

[1] J. K. Nørskov, J. Rossmeisl, A. Logadottir, L. Lindqvist, J. R. Kitchin, T. Bligaard and H. Jónsson, *J. Phys. Chem. B*, 2004, **108**, 17886–17892.

[2] S. Liu, Z. Li, C. Wang, W. Tao, M. Huang, M. Zuo, Y. Yang, K. Yang, L. Zhang, S. Chen, P. Xu and Q. Chen, *Nat. Commun*., 2020, **11**, 938.

[3] Z. Chen, X. Peng, Z. Chen, T. Li, R. Zou, G. Shi, Y. Huang, P. Cui, J. Yu, Y. Chen, X. Chi, K. P. Loh, Z. Liu, X. Li, L. Zhong and J. Lu, *Adv. Mater*., 2023, **35**, 2209948.

[4] H. Liu, L. Jiang, Y. Sun, J. Khan, B. Feng, J. Xiao, H. Zhang, H. Xie, L. Li, S. Wang and L. Han, *Adv. Funct. Mater*., 2023, **33**, 2304074.

[5] K. Kim, K. Min, Y. Go, Y. Lee, S. E. Shim, D. Lim and S.-H. Baeck, *Appl. Catal. B*, 2022, **315**, 121501.

[6] Y. Yan, B. Wen, M. Liu, H. Lei, J. Yang, S. He, Z. Qu, W. Xia, H. Li and J. Zeng, *Adv. Funct. Mater*., 2024, **34**, 2316100.

[7] M. Yu, F. Guo, L. Xu, Y. Zhang, W. Ni, J. Wang, Y. Wei, X. Chen, J. Yang, H. Li, J. Wang and J. Wang, *Adv. Funct. Mater*., 2025, **35**, 2411935.

[8] C. Lv, B. Li, Y. Ren, G. Zhang, Z. Lu, L. Li, X. Zhang, X. Yang and X. Yu, *Chem. Eng. J*., 2024, **495**, 153670.

[9] E. Zhu, T. Zheng, J. Yu, C. Shi, L. Zhou, H. Jin, J. Yang, G. Luo, D. Wei, X. Yang and M. Xu, *Energy Storage Mater*., 2024, **69**, 103410.

[10] J. Li, M. Lin, W. Huang, X. Liao, Y. Ma, L. Zhou, L. Mai and J. Lu, *Small Methods*, 2023, **7**, 2201664.

[11] X. Lin, Q. Li, Y. Hu, Z. Jin, K. M. Reddy, K. Li, X. Lin, L. Ci and H.-J. Qiu, *Small*, 2023, **19**, 2300612.

[12] X. Liu, F. Zhao, L. Jiao, T. Fang, Z. Zhao, X. Xiao, D. Li, K. Yi, R. Wang and X. Jia, *Small*, 2023, **19**, 2300289.

[13] M. Bu, Y. Liu, S. Liao, W. Liu, Z. Yang, J. Jiang, X. Gao, Y. Yang and H. Liu, *Carbon*, 2023, **214**, 118365.

[14] C. Mi, H. Yu, L. Han, L. Zhang, L. Zhai, X. Li, Y. Liu and Z. Xiang, *Adv. Funct. Mater*., 2023, **33**, 2303235.

[15] Y. Tian, Z. Wu, M. Li, Q. Sun, H. Chen, D. Yuan, D. Deng,B. Johannessen, Y. Wang, Y. Zhong, L. Xu, J. Lu and S. Zhang, *Adv. Funct. Mater*., 2022, **32**, 2209273.

[16] M. Shen, J. Liu, J. Li, C. Duan, C. Xiong, W. Zhao, L. Dai, Q. Wang, H. Yang and Y. Ni, *Energy Storage Mater*., 2023, **59**, 102790.

[17] J. Rong, E. Gao, N. Liu, W. Chen, X. Rong, Y. Zhang, X. Zheng, H. Ao, S. Xue, B. Huang, Z. Li, F. Qiu and Y. Qian, *Energy Storage Mater*., 2023, **56**, 165–173.

[18] T. Cui, Y.-P. Wang, T. Ye, J. Wu, Z. Chen, J. Li, Y. Lei, D. Wang and Y. Li, *Angew. Chem*., *Int. Ed*., 2022, **61**, e202115219.

[19] Q. Wang, Q. Feng, Y. Lei, S. Tang, L. Xu, Y. Xiong, G. Fang, Y. Wang, P. Yang, J. Liu, W. Liu and X. Xiong, *Nat. Commun*., 2023, **13**, 3689.

[20] J. Chen, C. Qiu, L. Zhang, B. Wang, P. Zhao, Y. Zhao, H. Wang, G. Yang, A. Sun, J. Fan, Q. Xv and O. J. Rojas, *Energy Environ. Sci*., 2024, **17**, 4746–4757.

[21] Y. He, H. Li, Y. Wang, Y. Jia, Y. Liu and Q. Tan, *J. Energy Chem*., 2024, **90**, 610–620.

[22] H. Sun, L. Li, Z. Zhu, X. Li, Z. Zhu, T. Yuan, J. Yang, Y. Pang and S. Zheng, *Chem. Eng. J*., 2024, **496**, 143669.

[23] Y. Yang, Y. Xiao, L. Zhang, H.-T. Wang, K.-H. Chen, W.-X. Lin, N. Jin, C. Sun, Y.-C. Shao, J.-L. Chen, J. Qian and L. Han, *Appl. Catal. B*, 2024, **347**, 123792.

[24] Y. Zhou, Y. Liu, Z. Wang, C. Li, Z. Wang, S. Zhang and C. Deng, *Energy Storage Mater*., 2023, **59**, 102772.

[25] L. Li, N. Li, J. Xia, S. Zhou, X. Qian, F. Yin, G. He and H. Chen, *J. Mater. Chem. A*, 2023, **11**, 2291–2301.

[26] H. Huang, A. Huang, D. Liu, W. Han, C.-H. Kuo, H.-Y. Chen, L. Li, H. Pan and S. Peng, *Adv. Mater*., 2023, **35**, 2303109.

[27] C. Ye, M. Zheng, Z. Li, Q. Fan, H. Ma, X. Fu, D. Wang, J. Wang and Y. Li, *Angew. Chem*., *Int. Ed*., 2022, **61**, e202213366.

[28] Y. Zhang, H. Qin, M. Alfred, H. Ke, Y. Cai, Q. Wang, F. Huang, B. Liu, P. Lv and Q. Wei, *Energy Storage Mater*., 2021, **42**, 88–96.

[29] Z. Pei, L. Ding, C. Wang, Q. Meng, Z. Yuan, Z. Zhou, S. Zhao and Y. Chen, *Energy Environ. Sci*., 2021, **14**, 4926–4935.

[30] D. Jiang, H. Wang, S. Wu, X. Sun and J. Li, *Small methods*, 2022, **6**, 2101043.

[31] B. Chen, H. Miao, M. Yin, R. Hu, L. Xia, C. Zhang and J. Yuan, *Chem. Eng. J*., 2021, **417**, 129179.

[32] J. Cui, M. Labbe, H.-J. Chung and D. G. Ivey, *J. Mater. Chem. A*, 2023, **11**, 13971–13983.

[33] M. Jiao, L. Dai, H.-R. Ren, M. Zhang, X. Xiao, B. Wang, J. Yang, B. Liu, G. Zhou and H.-M. Cheng, *Angew. Chem*., *Int. Ed*., 2023, **62**, e202301114.

[34] X. Han, N. Li, J. S. Baik, P. Xiong, Y. Kang, Q. Dou, Q. Liu, J. Y. Lee, C. S. Kim and H. S. Park, *Adv. Funct. Mater*., 2023, **33**, 2212233.

[35] L. An, B. Huang, Y. Zhang, R. Wang, N. Zhang, T. Dai, P. Xi and C.-H. Yan, *Angew. Chem., Int. Ed*., 2019, **58**, 9459–9463.

[36] J. Niu, Y. Liu, X. Wang, J. Liu, Z. Zhao, X. Liu and K. Ostrikov, *Small*, 2023, **19**, 2302727.